

## MULTISCALE MODEL OF TUMOR-DERIVED CAPILLARY-LIKE NETWORK FORMATION

MARCO SCIANNA

Department of Mathematics  
Politecnico di Torino  
Corso Duca degli Abruzzi 24  
10129, Torino, Italy

LUCA MUNARON

Department of Animal and Human Biology  
Nanostructured Interfaces and Surfaces Centre of Excellence (NIS)  
Center for Complex Systems in Molecular Biology and Medicine (SysBioM)  
Università degli Studi di Torino  
Via Accademia Albertina 13  
10123, Torino, Italy

(Communicated by Luigi Preziosi)

**ABSTRACT.** Solid tumors recruit and form blood vessels, used for maintenance and growth as well as for formation and spread of metastases. Vascularization is therefore a pivotal switch in cancer malignancy: an accurate analysis of its driving processes is a big issue for the development of treatments. *In vitro* experiments have demonstrated that cultured tumor-derived endothelial cells (TECs) are able to organize in a connected network, which mimics an *in vivo* capillary-plexus. The process, called *tubulogenesis*, is promoted by the activity of soluble peptides (such as VEGFs), as well as by the following intracellular calcium signals. We here propose a multilevel approach, reproducing selected features of the experimental system: it incorporates a continuous model of microscopic VEGF-induced events in a discrete mesoscopic Cellular Potts Model (CPM). The two components are interfaced, producing a multiscale framework characterized by a constant flux of information from finer to coarser levels. The simulation results, in agreement with experimental analysis, allow to identify the key mechanisms of network formation. In particular, we provide evidence that the nascent pattern is characterized by precise topological properties, regulated by the initial cell density in conjunction with the degree of the chemotactic response and the directional persistence of cell migration.

**1. Introduction.** In both physiological and pathological conditions, blood vessel formation and development is a complex and multiscale process, driven by the activation of endothelial cells (ECs) and essential for a myriad of biological phenomena (for a review, see [16]). Among others, the vascularization is a pivotal transition in cancer development. In fact by providing the nutrition and oxygen, it allows malignant cells to grow and remain viable, and, eventually, to cause metastases and enter

---

2000 *Mathematics Subject Classification.* Primary: 92B05, 92C15; Secondary: 92C42, 92C17.

*Key words and phrases.* Cellular potts model, *in vitro* tubulogenesis, vascular endothelial growth factor, proangiogenic calcium signals.

in the circulatory system [19]. The vascular transition is also active in determining the translation of dormant metastases to an aggressive status [18]. Indeed, the switch to the angiogenic phenotype leads to a fast progression and to a potentially fatal stage of fatal stage of the disease, representing therefore an important target for therapeutic interventions in most types of malignancies. However, despite the major progresses and promising successes achieved over the past few years in anti-angiogenic pharmacological therapies, several limitations still occur due to different factors, as commented in [18, 19, 26] and references therein.

A continuous effort in the development of biomedical therapies is advanced by multiple *in vitro* models, which are providing a deeper understanding of selected underpinning molecular and cellular events coordinated to control tumor-induced vessel formation, as reviewed in [3, 16, 59]. In particular, recent experimental investigations have demonstrated that, at the macroscopic morphological analysis, tumor blood vessels are irregular and dilated and that distinct venules, arterioles, and capillaries are un-distinguishable [23, 32]. Moreover, they differ from their “normal” counterpart by their altered blood flow and permeability, and by abnormalities in pericytes and in the basement membrane. Therefore, vascular endothelial cells deriving from tumors (TECs) represent a more adequate model for studying the mechanisms of malignant vascularization [5, 13, 38]. TECs have been isolated and cultured from human carcinomas on the basis of membrane markers and exhibit altered genotype, phenotype, and function. They are often aneuploid, display chromosomal instability and express peculiar genes [15, 63, 73]. In addition, tumor-derived ECs avoid senescence *in vitro* and show enhanced proliferation, motility and overexpression of membrane receptors [14, 15, 38]. As “normal” ECs, TECs cultured in Matrigel, a commercial product mimicking a natural basement membrane matrix, are able to autonomously organize to form a bidimensional tubular network, even in the absence of other cell types or positional cues [28], see Fig. 1. The overall patterning is complete within almost 12 hours, a characteristic time sufficiently distant from critical events, such as cell mitosis or death, that allows to assume the cell density conserved. The final structure, which can be geometrically described as a collection of nodes connected by homogeneously sized chords, is no longer substantially modified and resembles a primitive *in vivo* capillary-like plexus, see again [28]. The process, called *in vitro tubulogenesis*, is largely mediated by the activity of chemical morphogens (such as VEGF isoforms) that, similarly to the case of “normal” ECs (refer to [29, 56, 57, 58, 59]), exert a chemotactic force and, concomitantly, activate a series of calcium-dependent cascades, regulating the cells phenotypical behavior. In particular, a specific VEGF-induced protein cascades, involving protein kinase A, PKA, arachidonic acid, AA, and nitric oxide, NO (see Fig. 3) and resulting in an increase of intracellular calcium levels, due to the influx of the ion from the extracellular environment, has been well established and characterized in TEC models [28, 30].

The analysis performed on such experimental systems has revealed the role of different factors operating in malignant vascular progression. However, innumerable other mechanisms, acting at different scales, are far from being completely elucidated, and require a computational approach. Numerical models and simulations are able to replicate selected features of the *in vitro tubulogenesis*, allowing further insights of its driving processes. Indeed, in this work, we propose a theoretical multilevel model of the experimental TEC patterning. The cell population is described at the mesoscopic level with a discrete Cellular Potts Model (CPM), a

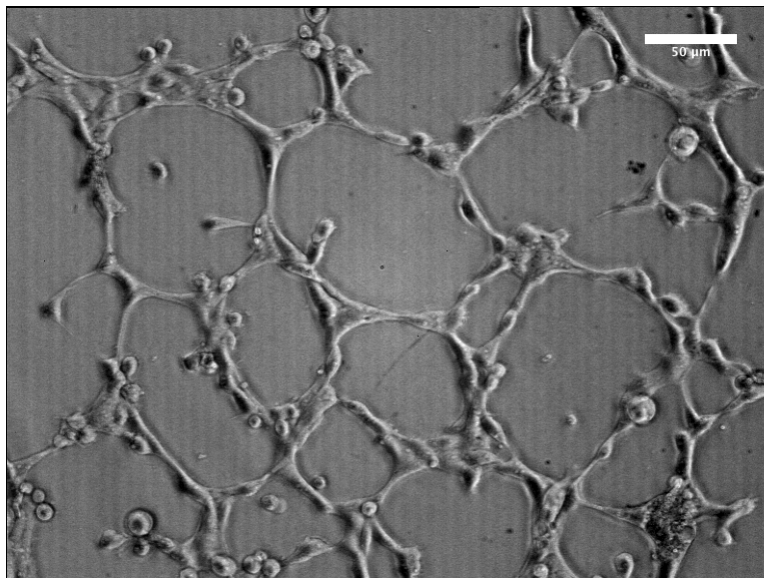


FIGURE 1. *In vitro* tubulogenesis of tumor-derived endothelial cells (TECs). Morphometry of the capillary-like network formed in 12 hours after cell incubation.

lattice-based Monte Carlo technique which follows an energy minimization philosophy and preserves the identity and the behaviors of single cells [4, 34, 35, 37, 49]. The microscopic VEGF-induced intracellular events are instead approached with a set of reaction diffusion equations. These two components are integrated and interfaced together, constituting a hybrid simulation environment characterized by a constant flux of information from finer to coarser levels, where the kinetics of the molecular sub-cellular network strongly influence the formation of the macroscopic multicellular network. Our model appears a possibly new and biologically interesting representative in the class of models of blood vessel development: from a biological view point, the characterization of tumor-derived endothelial cells, instead of “normal” endothelial cells, with their specific pathways represent an important development. Moreover, we here employ some interesting improvements and extensions of the CPM (explained in details in [72]): a more accurate representation of cells, differentiated in their nucleus and cytosolic region and the introduction of a new and more realistic Boltzmann-like probability function and, most relevantly, of the microscopic level. Indeed, different published CPMs have already focused on the *in vitro* vasculogenesis, providing that relatively simple cell-level mechanisms, such as adhesion [51], elongation [52], and contact-inhibited chemotaxis [53], are sufficient to obtain the organization of vascular cells into bidimensional networks. However, those works have approached the biological problem only from a phenomenological view point, prescribing to each individual a set of rules to follow during the entire patterning. The authors have therefore neglected the evolution of the internal state of the cells and of the intracellular dynamics (i.e., calcium signals, for example) that underlie their phenotypic behavior. At this regard, we here want to focus on the role played by the intracellular calcium level in affecting

both the biophysical and biomechanical properties of TECs and, eventually, the overall formation of the capillary-like structure. The model results reproduce with good accuracy the formation of a tumor capillary structure *in vitro* and are able to characterize its topological properties, with a close comparison with published experimental observations. In particular, through different sets of numerical realizations, we show that the initial density of the overall culture, as well as biophysical properties of single individuals, such as their calcium-dependent chemical and adhesive strength and the persistent component of their migration, play a fundamental role in determining the dynamic of network formation and its final configuration. Such a systematical analysis of the TEC pattern ability has the potential to propose biomedical approaches which are able to disrupt malignant neovascularization, as we provide elsewhere [71].

The rest of this paper is organized as follows. In Section 2, we clarify the assumptions on which our approach is based. We then show in Section 3, the model ability to reproduce accurate results with respect to biological evidence, These findings are finally discussed in Section 4.

**2. Mathematical model.** The proposed model spans the multiple levels involved in the tumor capillary-like network formation. Our approach incorporates in fact a continuous model of the specific VEGF-mediated intracellular cascades in a discrete phenomenological Cellular Potts Model, which considers TEC migration, adhesion and cytoskeletal remodeling. The different scales are thus integrated in a hybrid framework, and directly impact each others: cell biophysical properties are in fact realistically inherited by microscopic biochemical dynamics.

**2.1. Extended Cellular Potts Model.** The population of TECs is modeled at the mesoscopic level using an extended Cellular Potts Model, which realistically preserves the identity of single individuals, reproducing their behaviors and mutual interactions. All CPM domains are  $d$ -dimensional lattices (i.e., regular numerical repeated graphs, with  $d = 1, 2, 3$ ): however, since we wish to compare our simulations to experimental cultures, where the vascular patterns are essentially monolayers, in this work we use a bidimensional domain  $\Omega \subset \mathbb{R}^2$ . Each lattice site  $\mathbf{x}$  is labeled by an integer number,  $j(\mathbf{x})$ .  $j$  can be interpreted as a degenerate *spin* originally coming from statistical physics. Subdomains of contiguous sites with identical spin form discrete objects, which are also characterized by an object type,  $\tau(j)$ . As classically adopted in CPM models, a neighbor of site  $\mathbf{x}$  is identified with  $\mathbf{x}'$  while its overall neighborhood with  $\Omega'_{\mathbf{x}}$  (i.e.,  $\Omega'_{\mathbf{x}} = \{\mathbf{x}' \in \Omega : \mathbf{x}' \text{ is a neighbor of } \mathbf{x}\}$ ). As represented in Fig. 2, each simulated TEC,  $i$ , is defined as a compartmentalized unit, composed of two subregions which, in turn, are CPM objects: the cell nucleus, a central more or less round cluster of type  $\tau = N$ , whose location and geometry is estimated with experimental images, and the surrounding cytosol,  $\tau = C$ . Each compartment is also characterized, as an additional attribute, by the cluster id  $i$ , which obviously identifies the cell it belongs to. The TECs reside in a generalized substrate, a further discrete object of type  $\tau = M$ , which represents the experimental Matrigel. It is assumed to be static, passive and homogeneously distributed throughout the simulation domain, forming no large-scale structures as in [51, 52, 53]. The plasma and the nuclear envelopes are defined as the borders between the cell cytosolic compartment and, respectively, the medium and the nuclear region.

Simulated TECs move and evolve to iteratively and stochastically reduce a pattern free energy, given by an *hamiltonian*  $H$ , whose expression will be clarified

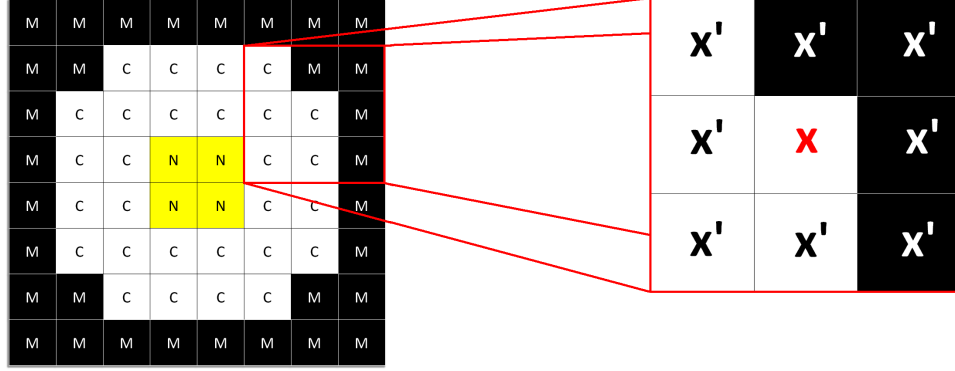


FIGURE 2. Representation of a compartmentalized cell  $i$ . Lattice sites of the nuclear region  $\tau(j(\mathbf{x}) = N)$  are in yellow, lattice sites of the cytosol in white  $\tau(j(\mathbf{x}) = C)$ . The extracellular Matrigel is labeled with  $\tau = M$ , and is colored in black. In the zoom view it is possible to see a sub-plasmamembrane lattice site and its first-nearest neighbors,  $\Omega'_x$ . The borders of  $\mathbf{x}$  in common with medium sites defined the cell plasmamembrane.

below. The core algorithm is a modified Metropolis method for Monte Carlo dynamics [37, 55], which is able to implement the natural exploratory behavior of cells, reproducing their cytoskeletally-driven membrane fluctuations and extensions of pseudopods. Procedurally, at each time step  $t$ , called Monte Carlo Step (MCS, the basic unit of time of the discrete model), a lattice site,  $\mathbf{x}_{source}$ , is selected at random and assigns its spin,  $j(\mathbf{x}_{source})$ , to one of its unlike neighbors,  $\mathbf{x}_{target}$ , also randomly selected. The net energy difference due to the proposed change of domain configuration,  $\Delta H|_{j(\mathbf{x}_{source}) \rightarrow j(\mathbf{x}_{target})} = H_{(after\ spin\ copy)} - H_{(before\ spin\ copy)}$ , is then evaluated. Finally, the trial spin update is accepted with an extended Boltzmann probability:

$$\begin{aligned} P(j(\mathbf{x}_{source}) \rightarrow j(\mathbf{x}_{target}))(t) &= \\ &= \tanh(T_{j(\mathbf{x}_{source})}(t)) \min\{1, e^{-\Delta H|_{j(\mathbf{x}_{source}) \rightarrow j(\mathbf{x}_{target})}/T_{j(\mathbf{x}_{source})}(t)}\}, \end{aligned} \quad (1)$$

where  $T_{j(\mathbf{x}_{source})}(t)$ , a Boltzmann temperature, is a sort of agitation rate of moving compartment  $j(\mathbf{x}_{source})$ . The specific form of (1) is identified so that it is possible to treat the cases of frozen or of low motility individuals, for which the probability of moving is null or limited even in the presence of favorable energy gradients, as commented in [72]. Specifically, for every cell  $i$  and for  $\tau(j(\mathbf{x}_{source})) = N$ ,  $T_{j(\mathbf{x}_{source})} = T_N$  is a constant low value mimicking the passive motion of the nucleus, which is dragged by the surrounding cytosolic region. For  $\tau(j(\mathbf{x}_{source})) = C$ ,  $T_{j(\mathbf{x}_{source})}(t)$  gives instead a measure of the intrinsic motility of  $i$ , which is enhanced by its intracellular calcium level, as provided by wound healing experiments [30]:

$$T_{j(\mathbf{x}_{source})}(t) = T_0 \left[ \frac{C^i(t)}{C_0^i + h(C^i(t) - C_0^i)} \right], \quad (2)$$

where  $C^i(t) = \sum_{\mathbf{x} \in i} C^i(\mathbf{x}, t)$  is the total calcium level inside cell  $i$ , the individual  $j(\mathbf{x}_{source})$  belongs to.  $C_0^i = \sum_{\mathbf{x} \in i} C_0^i(\mathbf{x}) = \sum_{\mathbf{x} \in i} C_0$  is the basal total amount of the

ion (the level below which the cell dies, for its estimation see the Appendix), while  $T_0$  corresponds to the basal motility of the TECs (i.e., in resting conditions), and  $T_0/h$  is their asymptotic motility for saturating  $\text{Ca}^{2+}$  concentrations. The specific form of (2) results in significative increments of cell motility in response to high intracellular levels of calcium (i.e., the asymptotic motility of individuals is twice its basal value): this choice is made to model the enhanced migratory capacities of TECs w.r.t. their “normal” counterparts upon agonist stimulations.

For any given time  $t$  the pattern free energy, whose minimization, as seen, drives the system evolution, is:

$$H(t) = H_{shape}(t) + H_{adhesion}(t) + H_{chemotaxis}(t) + H_{persistence}(t). \quad (3)$$

$H_{shape}$  models the geometrical attributes of cell subunits. They are written as non-dimensional relative deformations in the following quadratic form:

$$\begin{aligned} H_{shape}(t) &= H_{volume}(t) + H_{surface}(t) = \\ &= \sum_{i,j} \left[ \kappa_{i,j}(t) \left( \frac{v_{i,j}(t) - V_{\tau(j)}}{v_{i,j}(t)} \right)^2 + \nu_{i,j}(t) \left( \frac{s_{i,j}(t) - S_{\tau(j)}}{s_{i,j}(t)} \right)^2 \right], \end{aligned} \quad (4)$$

depending on the actual volume and surface of the compartments,  $v_{i,j}(t)$  and  $s_{i,j}(t)$ , as well as on the same quantities in the relaxed state,  $V_{\tau(j)}$  and  $S_{\tau(j)}$ , which correspond to the initial measures of cell nucleus and cytosol. The formulation of (4) allows to have finite energetic contributions, as well as a blow up in the case of  $v_{i,j}(t), s_{i,j}(t) \rightarrow 0$ . This means that for instance an infinite energy is needed to shrink a cell to a point.  $\kappa_{i,j}(t)$  and  $\nu_{i,j}(t)$  are energy penalties referring to cell mechanical moduli, which are in units of energy and directly related to intracellular microscopic quantities. In particular,  $\kappa_{i,j}(t) \in \mathbb{R}^+$  refers to volume changes of the relative compartment, while  $\nu_{i,j}(t) \in \mathbb{R}^+$  represents its inverse compressibility (its rigidity, i.e. the measure of the ease with which it is allowed to remodel). Assuming that TECs do not grow during patterning (we do not include any nutrients, as done in similar theoretical works [51, 52]), the fluctuations of their volume are kept negligible with high constant values of  $\kappa_{i,j} = \kappa_0$ , for any  $i$  and  $j$ . Moreover, cell nuclei have a low elasticity, and thus for  $j : \tau(j) = N$ ,  $\nu_{i,j} = \nu_N$  is another high constant quantity. Since intracellular calcium ions have been demonstrated to facilitate cytoskeletal reorganizations (refer to [8] and to [31], where the authors have specifically analyzed the influence of calcium signals on the actin dynamics in a TEC model), for any  $i$  and for  $j : \tau(j) = C$ , we set:

$$\nu_{i,j}(t) = \nu_0 \exp \left( -k \frac{C^i(t)}{C_0^i} \right), \quad (5)$$

where  $\nu_0$  is the intrinsic cells' resistance to compression at the basal calcium level,  $C_0^i$ , and  $C^i(t)$  is the actual total calcium amount of cell  $i$ , see (2).

$H_{adhesion}$  is the general extension of Steinberg's Differential Adhesion Hypothesis (DAH) [37, 77, 78]. In particular, it is differentiated in the contributions due to either the generalized contact between subunits belonging to the same cell, or the effective adhesion between membranes of different cells:

$$\begin{aligned} H_{adhesion}(t) &= H_{adhesion}^{int}(t) + H_{adhesion}^{ext}(t) = \\ &= \sum_{\mathbf{x}, \mathbf{x}'} \left[ J_{C,N}^{int}(\delta_{i(\mathbf{x}), i(\mathbf{x}')}(t))(1 - \delta_{j(\mathbf{x}), j(\mathbf{x}')}(t)) + J_{C,C}^{ext}(\mathbf{x}, \mathbf{x}', t)(1 - \delta_{i(\mathbf{x}), i(\mathbf{x}')}(t)) \right], \end{aligned} \quad (6)$$

where  $\mathbf{x}, \mathbf{x}'$  represent two neighboring lattice sites,  $\delta_{x,y} = \{1, x = y; 0, x \neq y\}$  is the Kronecher delta, and the  $J$ s are binding energies per unit of area. In particular,  $J_{C,N}^{int} \in \mathbb{R}^-$  is a constant high tension which prevents the cells from fragmenting.  $J_{C,C}^{ext}(\mathbf{x}, \mathbf{x}', t)$  represents instead the local adhesive strength of the interface  $\partial\mathbf{x} \cap \partial\mathbf{x}'$  between cells  $i$  and  $i'$ : from a statistical point of view it is a measure of the probability of the formation of local intercellular VE-cadherin-VE-cadherin complexes, which depends on the quantity of active exposed molecules on either sides of the interface. Since VE-cadherin activity is enhanced by calcium ions, which generate clusters of activated molecules, we set:

$$J_{C,C}^{ext}(\mathbf{x}, \mathbf{x}', t) = J_0 \exp\left(-p \frac{C^i(\mathbf{x}, t)C^{i'}(\mathbf{x}', t)}{C_0^i(\mathbf{x})C_0^{i'}(\mathbf{x}')}\right), \quad (7)$$

where  $C^i(\mathbf{x}, t)$  and  $C^{i'}(\mathbf{x}', t)$  are the local calcium levels, and  $C_0^i(\mathbf{x}) = C_0^{i'}(\mathbf{x}') = C_0$  the local basal concentration of the ion.  $J_0$  represents the typical adhesive force of resting TECs, estimated by qualitative observations of experimental cultures (see Appendix). Notice that we do not consider an adhesion energy between the cells and the simulated Matrigel, since such contact interactions do not play a major role in the early stages of the network formation (we remainder the reader to Sec. 4 for a more complete discussion).

$H_{chemotaxis}$  reproduces the effect of cell preferential movement in the direction of zones with higher concentration of morphogen, and is implemented with a local linear-type chemotactic term [69]:

$$\Delta H_{chemotaxis} = \mu_{ch}^i(\mathbf{x}_{source}, t) [Q(\mathbf{x}_{target}, t) - Q(\mathbf{x}_{source}, t)]. \quad (8)$$

$\mathbf{x}_{source}$  and  $\mathbf{x}_{target}$  are, respectively, the source and the final lattice site randomly selected during a trial update in a MCS, cf. (1), and, in particular,  $\mathbf{x}_{source}$  is a cytosolic site of cell  $i$  and  $\mathbf{x}_{target}$  is one of its neighboring medium sites.  $\mu_{ch}^i \in \mathbb{R}^+$  represents the local chemical sensitivity of the cell due to the activity of VEGF surface receptors, whose avidity is enhanced by free calcium ions:

$$\mu_{ch}^i(\mathbf{x}_{source}, t) = \mu_{ch,0} \left[ \frac{C_0^i(\mathbf{x}_{source}) + C^i(\mathbf{x}_{source}, t)}{C_0^i(\mathbf{x}_{source}) + q C^i(\mathbf{x}_{source}, t)} \right], \quad (9)$$

where  $\mu_{ch,0}$  is a basal intensity of the chemotactic response and  $Q(\mathbf{x}, t) = \sum_{\mathbf{x}'} V(\mathbf{x}', t)$ , where  $\mathbf{x} \in \{\mathbf{x}_{source}, \mathbf{x}_{target}\}$  and  $\mathbf{x}'$ , is a medium first-nearest neighbor of  $\mathbf{x}$ , evaluates the local extracellular level of VEGF sensed by the moving cell membrane site. Relation (9) is a strong improvement of this work w.r.t. in classic CPMs (see, for example [51, 52, 53]), as we briefly sketch in the following:

- in published CPM applications, all the cells of the same type feature the same chemical sensitivity, despite of their individuality and internal state (here defined by the intracellular calcium level);
- in those works, each single cell experiences a homogeneous chemotactic response over the entire membrane, hiding relevant microscopic inhomogeneities such as the clusterization of VEGF receptors or their local agonist-induced activation which, as we will see in Sec. 3, is fundamental for polarization mechanisms;
- finally, in the classical description, the chemical strengths are constant over time and they do not adapt during the simulated process. This is an un-plausible situation, since real cells constantly change their biophysical and

biomechanical properties as a consequence of continuous internal and external stimuli (we will comment this point again in Sec. 3).

The chemotactic response of TECs is similar, from a mechanical view point, to that of “normal” ECs, except from an enhanced magnitude, due to the overexpression to VEGF receptors [14, 38]: this is taken into account in (9) by setting an asymptotic chemical sensitivity which is twice of its basal level. Moreover, as in normal ECs, the TEC chemotactic strength is also mediated by active VE-cadherin molecules, which, as seen, cluster at cell-cell interfaces acting as local inhibitors of pseudopodal extensions. This mechanism, called *contact inhibition of chemotaxis*, has been widely demonstrated to be necessary for capillary network formation, and is modeled by imposing  $\mu_{ch} = 0$  at cell-cell interfaces as done in similar theoretical works [51].

Finally,  $H_{persistence}$  models the persistent motion characteristic of vascular cells:

$$H_{persistence} = \sum_i \mu_{pers}^i(t) \|\mathbf{v}_i(t) - \mathbf{v}_i(t - \Delta t)\|^2, \quad (10)$$

where  $\mathbf{v}_i$  is the instantaneous velocity of the center of mass of cell  $i$ , and  $\Delta t = 1$  MCS.  $\mu_{pers}$  controls the cell persistence time and is:

$$\mu_{pers}^i(t) = \mu_{pers,0} \left[ \frac{L^i(t)}{L_0} - 1 \right], \quad (11)$$

where  $L^i(t)$  is the current measure of the longer axis of cell  $i$ , and  $L_0$  is the initial cell diameter. (11) describes the fact that, after analogous chemical stimulations, elongated vascular cells have seen to have a longer persistent movement than round cells [41]. This is due to the increasing time needed by polarized actin filaments to reorient into a new direction. In particular,  $L^i(t) = L_0$  implies that  $\mu_{pers}^i(t) = 0$ , and thus that cell  $i$  is characterized by an uncorrelated Brownian motion.

TABLE I - PARAMETERS INVOLVED IN THE CELL-LEVEL MODEL

PARAMETER	DESCRIPTION	MODEL VALUE
$V_N$	area of nuclear compartment	130 [ $\mu\text{m}^2$ ]
$S_N$	perimeter of nuclear compartment	35 [ $\mu\text{m}$ ]
$V_C$	area of cytosolic compartment	1150 [ $\mu\text{m}^2$ ]
$S_C$	perimeter of cytosolic compartment	150 [ $\mu\text{m}$ ]
$T_0$	basal TEC motility	3.5
$T_N$	generalized motility of the nucleus	0.25
$h$	Michaelis-Menten coefficient for T	1/2
$\kappa_0$	volume elasticity of cell compartments	20
$\nu_N$	surface elasticity of nuclear compartment	20
$\nu_0$	intrinsic TEC elasticity	12
$k$	exponential coefficient for $\nu_{i,C}$	1
$J_{C,N}^{int}$	generalized nucleus-cytosol adhesion	-15 [ $\mu\text{m}^{-1}$ ]
$J_0$	basal adhesion strength	5 [ $\mu\text{m}^{-1}$ ]
$p$	coefficient for $J_{C,N}^{ext}$	1/2
$\mu_{ch,0}$	basal chemotactic strength	0.5
$q$	Michaelis-Menten coefficient for $\mu_{ch}$	1/2
$\mu_{pers,0}$	basal inertia strength	1.2

**2.2. Continuous model of VEGF-induced calcium-mediated dynamics.** To build a suitable model of proangiogenic chemical events in the TEC system, we start from the following set of assumptions, see Fig. 3 for a diagrammatic representation:

- VEGF is autocrinally released by TECs, and diffuses and degrades in a finite time throughout the extracellular environment;
- single molecules of morphogen are sequestered by the cells (via their surface tyrosine kinase receptors), and initiate a sequence of reactions culminating in the activation (via cAMP release) of protein kinase A (PKA), and the



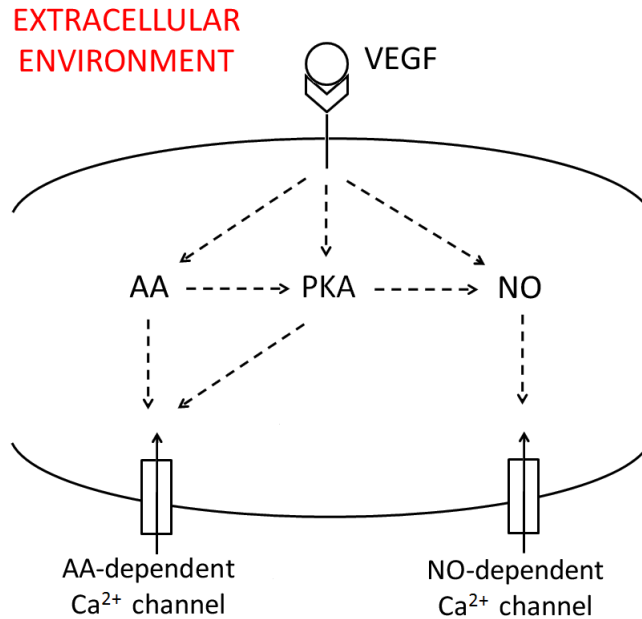


FIGURE 3. Schematic representation of VEGF-induced signaling cascades in the control of tumor-derived tubulogenesis. VEGF are internalized by tyrosine kinase receptors and activate a series of intracellular events inducing the activation of protein kinase A and the release of arachidonic acid (AA) and nitric oxide (NO) respectively. These intracellular messengers are then able to open plasma-membrane calcium channels leading to the efflux of the ion from the extracellular environment, refer to [28, 30].

production of arachidonic acid (AA) and nitric oxide (NO) in the sub plasmamembrane regions [42, 56, 57, 80];

- within cell cytosol NO production is triggered by PKA, whose recruitment, in turn, is AA-mediated;
- NO and AA open the relative and independent calcium channels in the cell plasmamembrane, leading to extracellular calcium entry [28, 29, 56, 57, 80, 83]. In particular, in the activity of AA-dependent channels a permissive role is played by PKA [30, 56, 57];
- calcium ions, reversibly buffered to proteins such as calmodulin or to mitochondria [7, 9, 43], can be extruded back from cell by plasmamembrane calcium ATPase and Ca<sup>2+</sup>-Na<sup>+</sup> exchangers [36, 40, 82].

2.2.1. *Evolution of intracellular chemicals.* Following the above clarified hypothesis, for each cell  $i$ , the current levels of PKA,  $P^i(\mathbf{x}, t)$ , AA,  $A^i(\mathbf{x}, t)$ , and NO,  $N^i(\mathbf{x}, t)$ , are controlled by a system of reaction-diffusion equations, which model

their biosynthesis, diffusion within the cytosol, and natural decay:

$$\left\{ \begin{array}{l} \frac{\partial A^i(\mathbf{x}, t)}{\partial t} = \underbrace{D_A \nabla^2 A^i(\mathbf{x}, t)}_{diffusion} - \underbrace{\lambda_A A^i(\mathbf{x}, t)}_{decay} \quad \text{in } i; \\ A^i(\mathbf{x}, t) = \alpha_A \frac{r(\mathbf{x}, t)}{\beta_A + r(\mathbf{x}, t)} \quad \text{at the internal boundary of } i; \\ \frac{\partial P^i(\mathbf{x}, t)}{\partial t} = \underbrace{D_P \nabla^2 P^i(\mathbf{x}, t)}_{diffusion} - \underbrace{\lambda_P P^i(\mathbf{x}, t)}_{decay} + \underbrace{\gamma_P \frac{A^i(\mathbf{x}, t)}{\zeta_P + A^i(\mathbf{x}, t)}}_{AA\text{-induced production}} \quad \text{in } i; \\ P^i(\mathbf{x}, t) = \alpha_P \frac{r(\mathbf{x}, t)}{\beta_P + r(\mathbf{x}, t)} \quad \text{at the internal boundary of } i; \\ \frac{\partial N^i(\mathbf{x}, t)}{\partial t} = \underbrace{D_N \nabla^2 N^i(\mathbf{x}, t)}_{diffusion} - \underbrace{\lambda_N N^i(\mathbf{x}, t)}_{decay} + \underbrace{\gamma_N \frac{P^i(\mathbf{x}, t)}{\zeta_N + P^i(\mathbf{x}, t)}}_{PKA\text{-mediated production}} \quad \text{in } i; \\ N^i(\mathbf{x}, t) = \alpha_N \frac{r(\mathbf{x}, t)}{\beta_N + r(\mathbf{x}, t)} \quad \text{at the internal boundary of } i; \end{array} \right. \quad (12)$$

where  $D_z$  and  $\lambda_z$  with  $z = P, A, N$  are, respectively, the diffusion coefficients and the degradation rates of the chemical messengers, which are homogeneous and constant in cell cytosolic region. The boundary conditions in the system (12) describe the production/activation, at the internal part of cells membranes, of the signal transduction substances, which is mediated by the number of sequestered VEGF molecules, given by

$$r(\mathbf{x}, t) = \sum_{\mathbf{x}' \in \Omega_x^i : \tau(j(\mathbf{x}')) = M} B(\mathbf{x}', t), \quad (13)$$

where  $B(\mathbf{x}', t)$  will be defined in details below, see Eq. (19). The last term in the equation of PKA evolution models its AA-induced recruitment, while the last term in the equation of for NO dynamics accounts for its biosynthesis, mediated by AA via PKA itself: both are described by other saturating functions. In model (12), we do not include the kinetics of multiple signal transduction proteins, that are known intermediates in VEGF-induced pathways, but that do not strongly influence their final outcome. Moreover, notice that the the volume of each cell  $i$ , as well as its boundary, is time-dependent at it may deform at each MCS.

For each cell  $i$ , the intracellular level of calcium,  $C^i(\mathbf{x}, t)$ , is determined by a balance of entry, extrusion, and buffering [27, 60, 76]:

$$\left\{ \begin{array}{l} \frac{\partial C^i(\mathbf{x}, t)}{\partial t} = K_{buff} \underbrace{D_C \nabla^2 C^i(\mathbf{x}, t)}_{diffusion} \quad \text{in } i; \\ n_{\mathbf{x}} \cdot \nabla C^i(\mathbf{x}, t) = \underbrace{F_A^i(\mathbf{x}, t) + F_N^i(\mathbf{x}, t)}_{influxes} - \underbrace{F_{out}^i(\mathbf{x}, t)}_{efflux} \quad \text{at the internal boundary of } i, \end{array} \right. \quad (14)$$

where  $n_{\mathbf{x}}$  is the unit outward normal to the external boundary of site  $\mathbf{x}$ . The coefficient of diffusion,  $D_C$ , is assumed to be homogeneous throughout all cell subunits (the diffusion of calcium across the nuclear envelope is taken to occur through non selective pores, whose permeability is proportional to the diffusion constant of the ion in the cytosol [22, 60]), while the scaling factor  $K_{buff} = \frac{K_{off}}{K_{off} + K_{on}b_T}$  models the activity of intracellular endogenous buffers, which have a significant impact on the overall calcium dynamics, contributing to decrease the level of the ion [1, 9, 10, 12]. In particular,  $b_T$  is the total concentration of buffer sites (considered constant and experimentally estimated in different cell types),  $K_{on}$  is the rate of calcium uptake,  $K_{off}$  the rate of its release. However, the value of  $K_{buff}$  will be discussed in the Appendix. For each individual, the calcium fluxes with the extracellular environment are considered as boundary conditions. In particular, the overall calcium efflux from cell  $i$  incorporates the extrusion of the ion both via PM ATP-ase and  $\text{Ca}^{2+}$ - $\text{Na}^{2+}$  exchangers. In order to avoid over-complications, we approximate its total rate as a single Michaelis-Menten form:

$$F_{out}^i(\mathbf{x}, t) = k_C \left[ \frac{C^i(\mathbf{x}, t)}{C_{out} + C^i(\mathbf{x}, t)} \right], \tag{15}$$

where  $k_C$  is the maximal rate of calcium extrusion, and  $C_{out}$  the calcium concentration at which the rate of efflux is half maximal.  $F_A^i$ , and  $F_N^i$  model the  $\text{Ca}^{2+}$  influx distributions from the extracellular environment through independent channels, which are assumed to be saturably dependent on the concentration of the relative second messenger:

$$F_A^i(\mathbf{x}, t) = F_{A,max} \left[ \frac{P^i(\mathbf{x}, t)A^i(\mathbf{x}, t)}{q_A + A^i(\mathbf{x}, t)} \right]^2; \tag{16}$$

$$F_N^i(\mathbf{x}, t) = F_{N,max} \left[ \frac{N^i(\mathbf{x}, t)}{q_N + N^i(\mathbf{x}, t)} \right]^2. \tag{17}$$

We use a quadratic exponent to fit experimental fluxes measured in [30, 56, 60]. Notice that (16) takes into account of the permissive role played by PKA in the activity of the AA-dependent channels. In our approach we neglect the existence of co-modulated channels and of potential cross regulations between them. Moreover, we assume no calcium flows across intercellular membranes.

2.2.2. *Evolution of extracellular chemicals.* The extracellular spatial profile of VEGF,  $V(\mathbf{x}, t)$  satisfies:

$$\left\{ \begin{array}{ll} \frac{\partial V(\mathbf{x}, t)}{\partial t} = \underbrace{D_V \nabla^2 V(\mathbf{x}, t)}_{diffusion} - \underbrace{\lambda_V V(\mathbf{x}, t)}_{degradation} & \text{outside cells;} \\ V(\mathbf{x}, t) = \underbrace{\phi_V}_{production} - \underbrace{B(\mathbf{x}, t)}_{consumption} & \text{at the external boundary of cells;} \\ n_{\mathbf{x}} \cdot \nabla V(\mathbf{x}, t) = 0 & \text{at the boundary of domain } \Omega. \end{array} \right. \tag{18}$$

$D_V$  and  $\lambda_V$  are, respectively, the diffusion coefficient and the characteristic degradation rate of the growth factor, which are homogeneous throughout the simulated Matrigel [74]. The release of VEGF from TEC membranes is at a constant rate  $\phi_V$  per unit of time, see also [74].  $B$  models instead the amount of VEGF that

is sequestered by cell surface tyrosine kinase receptors. Locally, it is the smallest between the actual available molecular concentration  $V$  and the maximal amount of VEGF that can be captured by the cells per unit of time [6, 47], which we define with  $\beta_V$  and whose estimation will be clarified in the Appendix:

$$B(\mathbf{x}, t) = \min\{\beta_V, vV(\mathbf{x}, t)\}, \quad (19)$$

where pre-factor  $v$  is in units of time.

Finally, the extracellular level of calcium evolves according to:

$$\left\{ \begin{array}{l} \frac{\partial C^{ext}(\mathbf{x}, t)}{\partial t} = \underbrace{D_C \nabla^2 C^{ext}(\mathbf{x}, t)}_{diffusion} \quad \text{outside cells;} \\ n_{\mathbf{x}} \cdot \nabla C^{ext}(\mathbf{x}, t) = \sum_{\mathbf{x}' \in \Omega'_{\mathbf{x}}: \tau(j(\mathbf{x}'))=C} \left[ \underbrace{-F_A^i(\mathbf{x}', t) - F_N^i(\mathbf{x}', t)}_{fluxes\ to\ cells} + \underbrace{F_{out}^i(\mathbf{x}', t)}_{fluxes\ from\ cells} \right] \\ \quad \text{at the external boundary of cells;} \\ n_{\mathbf{x}} \cdot \nabla C^{ext}(\mathbf{x}, t) = 0 \quad \text{at the boundary of domain } \Omega, \end{array} \right. \quad (20)$$

where, as usually,  $n_{\mathbf{x}}$  is the unit outward normal to the external boundary of site  $\mathbf{x}$ . In particular, we use no-flux conditions at the external boundary of the domain, while the other flux distributions are characterized in Eq. (14).

TABLE II - PARAMETERS INVOLVED IN THE MICROSCOPIC MODEL

PARAMETER	DESCRIPTION	MODEL VALUE
$D_V$	VEGF diffusion constant	10 [ $\mu\text{m}^2\text{s}^{-1}$ ]
$\lambda_V$	VEGF on-rate degradation constant	$1.8 \cdot 10^{-4}$ [ $\text{s}^{-1}$ ]
$\phi_V$	VEGF on-rate secretion constant	0.78 [ $\text{h}^{-1}$ ]
$\beta_V$	maximal rate of VEGF internalization	0.06 [ $\text{pg}/\text{cell}/\text{h}$ ]
$v$	VEGF internalization coefficient	1 [ $\text{h}^{-1}$ ]
$D_A$	AA diffusion constant	10 [ $\mu\text{m}^2\text{s}^{-1}$ ]
$\lambda_A$	AA on-rate secretion constant	30 [ $\text{s}^{-1}$ ]
$\alpha_A$	maximal rate of VEGF-dependent AA release	30 [ $\mu\text{M}\text{s}^{-1}$ ]
$\beta_A$	Michaelis-Menten constant for VEGF-dependent AA release	1 [ $\mu\text{M}$ ]
$D_P$	PKA diffusion constant	30 [ $\mu\text{m}^2\text{s}^{-1}$ ]
$\lambda_P$	PKA on-rate degradation constant	23 [ $\text{s}^{-1}$ ]
$\alpha_P$	maximal rate of VEGF-dependent PKA release	30 [ $\mu\text{M}\text{s}^{-1}$ ]
$\beta_P$	Michaelis-Menten constant for VEGF-dependent PKA release	1 [ $\mu\text{M}$ ]
$\gamma_P$	maximal rate of AA-dependent PKA recruitment	30 [ $\mu\text{M}\text{s}^{-1}$ ]
$\zeta_P$	Michaelis-Menten constant for AA-dependent PKA recruitment	1 [ $\mu\text{M}$ ]
$D_N$	NO diffusion constant	3300 [ $\mu\text{m}^2\text{s}^{-1}$ ]
$\lambda_N$	NO on-rate degradation constant	0.1 [ $\text{s}^{-1}$ ]
$\alpha_N$	maximal rate of VEGF-dependent NO release	30 [ $\mu\text{M}\text{s}^{-1}$ ]
$\beta_N$	Michaelis-Menten constant for VEGF-dependent NO release	1 [ $\mu\text{M}$ ]
$\gamma_N$	maximal rate of NO release	1.5 [ $\mu\text{M}\text{s}^{-1}$ ]
$\zeta_N$	dissociation constant between PKA and eNOS	0.5 [ $\mu\text{M}$ ]
$C_0$	basal cell calcium level	0.05 [ $\mu\text{M}$ ]
$C_{ext,0}$	extracellular calcium level	2000 [ $\mu\text{M}$ ]
$D_C$	diffusion constant of Ca	220 [ $\mu\text{m}^2\text{s}^{-1}$ ]
$k_C$	maximal rate of calcium efflux	24.7 [ $\mu\text{M}\text{s}^{-1}$ ]
$C_{out}$	threshold concentration for calcium extrusion	0.32 [ $\mu\text{M}$ ]
$F_{A,max}$	maximal rate of AA-dependent calcium influx	6 [ $\text{s}^{-1}$ ]
$F_{N,max}$	maximal rate of NO-dependent calcium influx	4.5 [ $\text{s}^{-1}$ ]
$q_A$	Michaelis-Menten constant for AA-dependent influx	2 [ $\mu\text{M}$ ]
$q_N$	Michaelis-Menten constant for NO-dependent influx	5 [ $\mu\text{M}$ ]
$K_{off}$	dissociation constant between buffers and $\text{Ca}_c$	300 [ $\text{s}^{-1}$ ]
$K_{on}$	on-rate constant of $\text{Ca}_c$ buffering	100 [ $\mu\text{M}^{-1}\text{s}^{-1}$ ]
$b_T$	total buffer concentration	450 [ $\mu\text{M}$ ]

**3. Simulations and results.** Our model framework is implemented with a modified version of the open-source CompuCell3D<sup>1</sup> environment [35, 67], which is able to integrate all the proposed biological submodels, while maintaining their modularity. The grid for the numerical solution of the PDEs is in fact matched with the CPM lattice while, at every time step, each computational module is used as the initial condition for the others. Indeed, the main lines of the computational algorithm are as follows:

- the discrete CPM evolves through a MCS, following the rules given in Eq. (1);
- the local quantities of the chemicals are computed, basing on the new cell configuration. In particular, after the *spin flip*, the target site,  $\mathbf{x}_{target}$ , is assigned the same concentrations of the chemicals as the moving source site,  $\mathbf{x}_{source}$ . For example, if a medium site  $\mathbf{x}_{target}$  is occupied by a site,  $\mathbf{x}_{source}$ , belonging to cell  $i$ , it results that  $A^i(\mathbf{x}_{target}, t) = A^i(\mathbf{x}_{source}, t)$ ,  $N^i(\mathbf{x}_{target}, t) = N^i(\mathbf{x}_{source}, t)$ ,  $P^i(\mathbf{x}_{target}, t) = P^i(\mathbf{x}_{source}, t)$  and  $C^i(\mathbf{x}_{target}, t) = C^i(\mathbf{x}_{source}, t)$ , while, obviously,  $V(\mathbf{x}_{target}, t) = 0$ ;
- the continuous equations of the chemicals are rederived, according the new distribution of the chemicals themselves and to the new cell boundaries, and solved, using a finite element scheme, characterized by 10 diffusion time steps per MCS (this temporal step is sufficiently small to guarantee numerical stability);
- the biophysical properties of each individual (i.e., Eqs. (2), (5), (7), (9), and (11)) are updated, given its new intracellular state and the new configuration of the lattice;
- the Hamiltonian functional in Eq. (3) is updated, and the system is ready to evolve again.

The domain  $\Omega$  consists in a  $500 \times 500$  square lattice, where each site is equivalent to  $4 \mu\text{m}^2$ .  $\Omega$  therefore represents a section of a 24-well plate of size  $L_\Omega = 1 \text{ mm}$ . The experimental time is set to 10 s per MCS: for this choice the simulated TECs move with nearly the experimental velocity of vascular cells ( $\approx 25 \mu\text{m}/\text{h}$  [53, 65]) and the overall patterning has a comparable time scale ( $\approx 12 \text{ h}$  [28]). Initially, we randomly distribute  $n = 150$  TECs in  $\Omega$ , reproducing a typical experimental cell density [28]. Each individual has an un-polarized morphology with a diameter of  $40 \mu\text{m}$  (20 lattice sites), while its nucleus is a central and round cluster of  $6 \mu\text{m}$  (3 sites) of radius: these measures agree with the most usual geometries observed in *in vitro* TEC cultures [28, 30]. A single cell is therefore a moving subdomain, which extends over an area of nearly 320 sites ( $\approx 1280 \mu\text{m}^2$ ): such a spatial resolution allows to have a good approximation in the resolution of the spatio-temporal intracellular dynamics without slowing down too much the speed computational machinery. Cells do not undergo mitosis or death during the entire simulations: in this way, consistently with the experimental observations given in Sec. 1 and with other similar approaches [51, 52, 53], the density of the culture is conserved during the overall process. The biological variables are initiated at their physiological levels: in particular, there are no activated second messengers within the cells, and the intracellular basal calcium concentration is assumed to be spatially homogeneous (see Appendix). In the extracellular domain, the initial level of  $\text{Ca}^{2+}$  is set equal to  $C_{ext,0}$ , while there are no VEGF molecules. All others model parameters are listed in Tables I and II.

<sup>1</sup><http://www.compuCell3d.org>

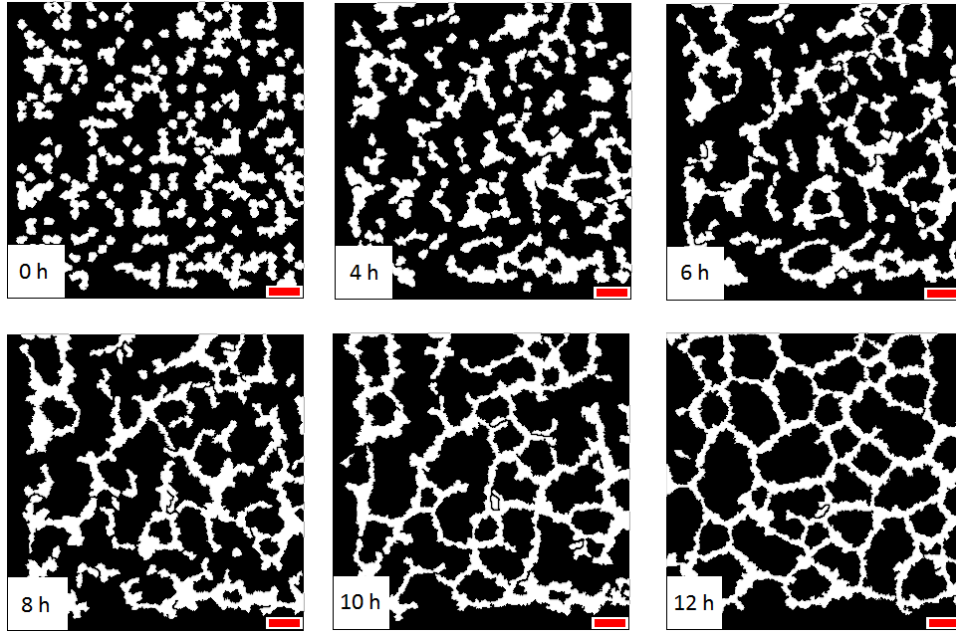


FIGURE 4. Tumor-derive capillary-like network formation. The simulation initiates with 150 quiescent TECs over domain  $\Omega$ , a square lattice of size  $L_{\Omega} = 1$  mm. Representative images show a time-sequence of the tubule organization. Red scale bar is  $100 \mu\text{m}$  long.

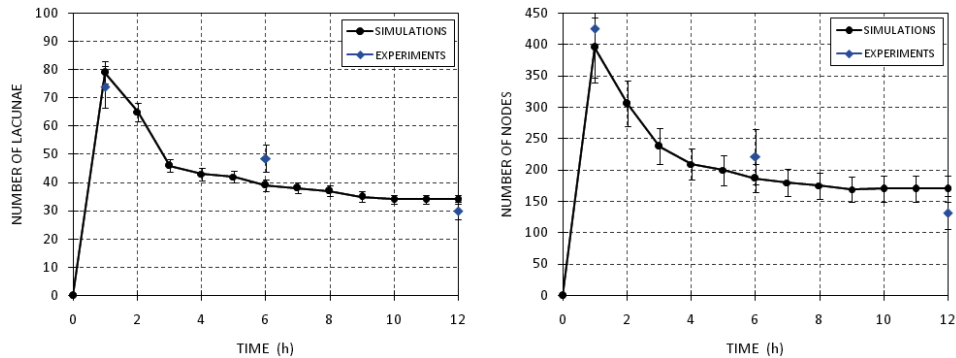


FIGURE 5. Dynamical evolution of TEC network formation. Time-evolution of the number of lacunae and the number of nodes during patterning in both simulations and experiments. Error bars for computational values show standard deviations over 20 simulations, while errors bars for experimental values show standard deviations over 8 realizations. *In vitro* data have been evaluated from experimental images periodically recorded (i.e., at 6 h-intervals) during tubulogenic processes of cultures of endothelial cells derived from human breast carcinomas (B-TECs), seeded onto Matrigel-coated wells and stimulated with angiogenic factors, as provided in [28].

The model results provide a remarkable agreement with experimental observation, both in the final pattern structure, see Figs. 4 and 1 for a comparison, and in the dynamical evolution, see Fig. 5. In particular, simulated TECs autonomously organize into a typical capillary-like plexus, where connected one-two cells-wide chords enclose lacunae, which are almost uniform in size. Information about the overall pattern formation are instead obtained by counting the numbers of nodes and lacunae at different times: as represented in Fig. 5 both of them quickly drop and then slowly stabilize. This is due to the fact that the smaller lacunae shrink and collapse and the unstructured cellular branches adhere and align to form a single structure. As a further quantitative analysis of the formed network, we measure its average metric and topological properties. The pattern features typical intercapillary distances (i.e., the mean diameters of lacunae) ranging from  $120 \mu\text{m}$  to  $250 \mu\text{m}$ , and a mean chord length (measured as the segment from one node to another) of  $180 \pm 10 \mu\text{m}$ . The geometrical description of the emerging structure is in good agreement with the experimental analysis provided in [28] on a culture of endothelial cells derived from human breast carcinomas (B-TECs), plated on a growth factor-reduced Matrigel and stimulated with angiogenic factors. Moreover, the network sizes captured by our model are surprisingly consistent also with those measured in the case of tubulogenic assays performed with “normal” endothelial cells (i.e., HUVECs, human umbilical vein EC, see [74]). In particular, these natural length scales have been demonstrated to be dictated by the effective range of cell-to-cell interactions, which is mediated by the release of the soluble VEGF (in particular by its diffusion coefficient and decay rate, see again [74]). Such characteristic measures of a bidimensional capillary pattern (both tumor-derived or “normal”) are biologically functional and instrumental for an optimal metabolic exchange: a coarser structure would be in fact unable to differentiate to form the lumen, while an immature and finer net would be obviously usefulness, refer to [21, 39].

Focusing on the trajectory of single cells, similarly to the experimental pictures in [74] for HUVECs, Figure 6 shows that the motion is directed towards zones of higher concentrations of morphogen, maintaining a directional persistence: a random component is of course present, however it is not predominant. Such a characteristic migration, which is the combination of chemotaxis and persistence, has been experimentally demonstrated to be fundamental to produce capillary chords in physiological cases as well, while the slower sideaway fluctuations of cells have been shown to be responsible of pattern coarsening, when single branches connect each other forming a structured network [53, 74]. Figure 6 captures also the elongation process of TECs, which undergo a gradual transition from the initial round stationary state to a migratory bipolar morphology, with clearly distinguishable leading and trailing surfaces dictating the direction of motion. It is useful to underline that the polarization of migrating individuals has not required any *a priori* assumptions or prescribed rules on their length (as commonly done in similar models, see [52]). In the presented approach, it in fact emerges as the natural result of the interplay between the local chemotactic-induced membrane extension at the front of the cells (impossible with the homogeneous chemical strength used in those approaches) and the mechanical properties given to their compartments, with a stiff nucleus and a more fluid cytoplasm. In particular, the exogenous stimulus causes the cell plasmamembrane to locally protrude in the direction of increasing VEGF gradients, with a speed of protrusion proportional to the modulus of the local chemical strength itself (for instance, in any CPM model the simulated objects

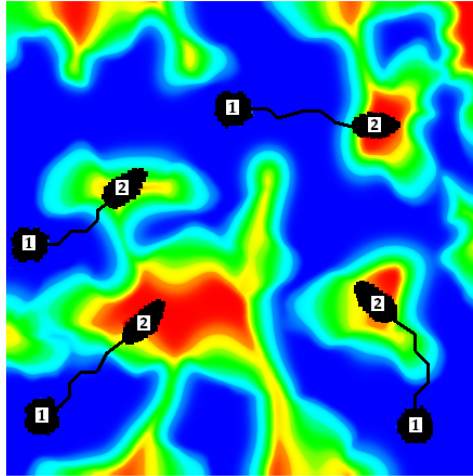


FIGURE 6. Magnification of four representative single-TEC motion trajectories obtained from a time-lapse simulation. The initial (i.e., at 0 h) position of individuals is labeled with 1, while the final (i.e., at 12 h) with 2. Each segment tracks a displacement of 2 hours. In the background the concentration field of VEGF is pseudocolor-scaled so that the maximum level is red and minimum level is blue. The TECs move in the directions of higher morphogen concentrations, displaying a persistent directional migration. The image also captures the polarization process typical of vascular cells: it is useful to underline that cell elongation is realistically reproduced in the model, as it emerges as the natural consequence of the interplay between the calcium-induced reorganization of the cell cytoskeleton and the VEGF chemotactic stimulus.

experience an implicit drag force from the lattice, and thus they have Aristotelian dynamics, refer to [4, 50] for more detailed comments). Pushed by the leading front, the overall cytosolic region, whose elasticity and mobility increase due to the concomitantly calcium accumulation, then deforms and moves forward, while pulling onto the nucleus with the same force. The nucleus (which, as a CPM object, also follows Aristotelian dynamics), as a consequence of its rigidity, moves with a lower velocity than the surrounding cytosol and lags behind, creating the polarized morphology (see [70] for a detailed explanation).

The model allows also an accurate analysis of intracellular calcium events during the overall tubulogenic process. In particular, as depicted in Fig. 7, our simulations show that VEGF-evoked  $\text{Ca}^{2+}$  signals are clearly detectable in the early phases of the patterning, when TECs are not well connected in a mature network, while when the tubules are more structured they are significantly downregulated. The peculiar temporal evolution of calcium signals has been observed also in *in vitro* assays [28] and may play a specific role in transducing information during the different phases of the process [59]. At this regard, even though experimental models have not yet shed light on the molecular mechanisms underlying such a decay in calcium events, our approach could suggest a simple and plausible functional explanation. The initial dramatic increase in intracellular calcium levels is in fact necessary for the enhancement of cell migratory properties (see Eqs. (2) and (9)), which is in turn fundamental in the first stages of the patterning, as the TECs have to efficiently



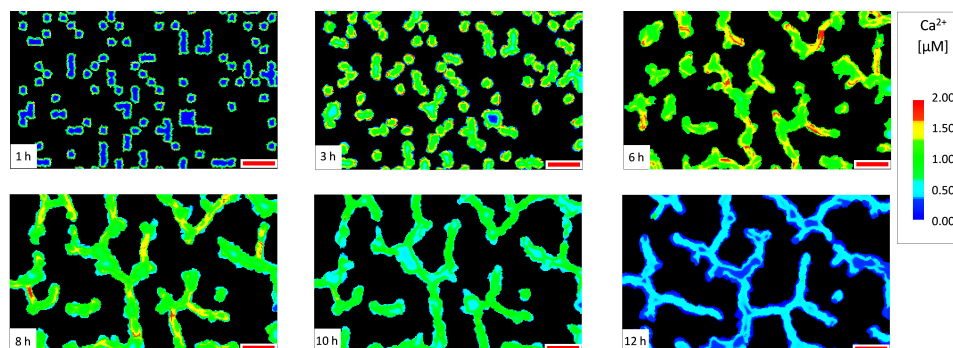


FIGURE 7. Time-evolution of VEGF-induced intracellular calcium dynamics. Calcium signals are clearly detectable at the early stages of tumor capillary-like formation, while they are down-regulated in the final phases of the process, when the network is more structured. Red scale bar is  $100 \mu\text{m}$  long.

move and interact. Subsequently, when the network is mature, the positions of cells are stabilized in the structure and, without the necessity of a significant further locomotion, their migratory capacities can be partially inactivated and, therefore, the cytosolic  $\text{Ca}^{2+}$  can decrease until almost its basal level. It is useful to notice that the use of a constant chemotactic strength (i.e., as in classical CPMs) would have unrealistically affected the stabilization of the structure, since the cells would have continued to move following the external chemical stimulus, likely detaching from each other. The regulation of  $\text{Ca}^{2+}$ -dependent mechanisms may thus represent an important target for therapeutic strategies, which aim at disrupting malignant vascularization and, eventually, at inhibiting tumor development as experimentally provided in [61, 64] and theoretically demonstrated by us in [71].

Up to now we have shown the model ability to start from realistic initial data and foresee the dynamics of tumor tubulogenesis consistently with respect to published experimental works. We now focus on the pattern dependence from some critical quantities. First, we perform simulations by varying the initial cell number, see Figs. 8 and 9. Below a critical value,  $n \leq n_{c1} = 100$ , we observe the formation of groups of disconnected structures, while, by increasing  $n$ , a single connected network forms. In particular, for a wide range of cell densities,  $n \in (100 ; 300)$ , the typical length of chords and size of lacunae remain approximately fixed, while the chord thickness grows to accommodate the increasing number of cells, and, consequently, the number of lacunae slightly decreases. Finally, for  $n > n_{c2} = 300$ , we find a continuous carpet of cells interspersed by holes. Interestingly, this phenomenon resembles to the *percolative and Swiss cheese transitions* observed in the development of physiological vasculatures [33, 74]: therefore such a topological property is of biological relevance also for tumor-derived vascular cells, and may be directly linked to the efficiency of the nascent capillary plexus.

As a further validating prediction, we study TECs organization in the case of a direct inhibition of the chemotactic mechanism, by imposing  $\mu_{ch}^i = 0$  for each cell  $i$  in Eq. (8). As represented in Fig. 10A, the resulting simulation reproduces a clear disruption of network assembly, with the formation of poorly structured vascular islands, similar to those experimentally obtained by extinguish VEGF gradients, for example, in the case of “normal” ECs, by adding saturating amounts of exogenous

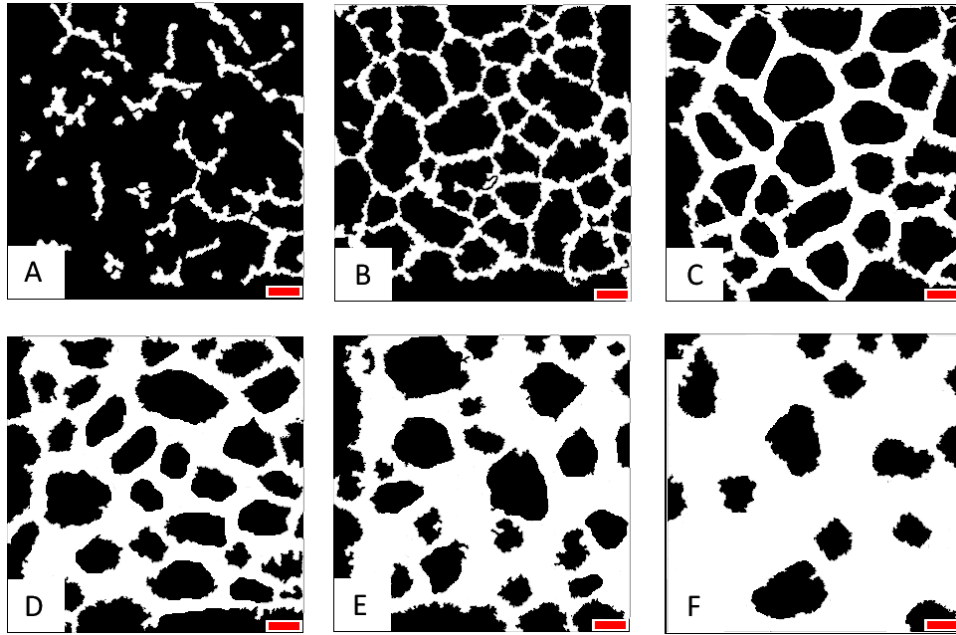


FIGURE 8. Percolative property of tumor-derived endothelial cells. Final patterns (i.e., after 12 h) formed by initially different numbers of cells. (A)  $n=50$ , (B)  $n=150$ , (C)  $n=200$ , (D)  $n=300$ , (E)  $n=400$ , and (F)  $n=500$ . Except from the initial cell density all simulations use the same standard parameter setting of the realization in Fig. 4. Red scale bar is  $100 \mu\text{m}$  long.

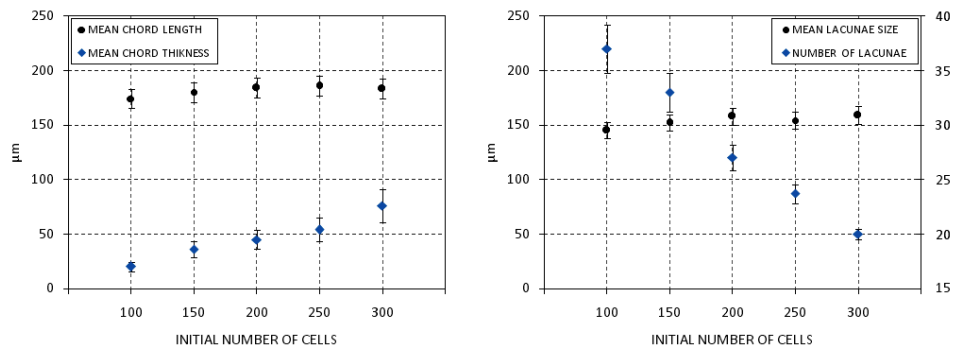


FIGURE 9. Percolative and “Swiss cheese” transition of tumor-derived endothelial cells. Topological properties of the pattern as a function of the initial cell density. Error bars show standard deviation over 20 simulations.

morphogen [52, 53, 74]. In particular, an accurate analysis of cell tracks shows that, although maintaining a certain degree of directional persistence (due to the term  $H_{pers}$  in (3)), cell movement is completely uncorrelated from the directions of chemical gradients, see Fig. 10B. In particular, migrating individuals feature an un-polarized morphology during the entire patterning: without experiencing the

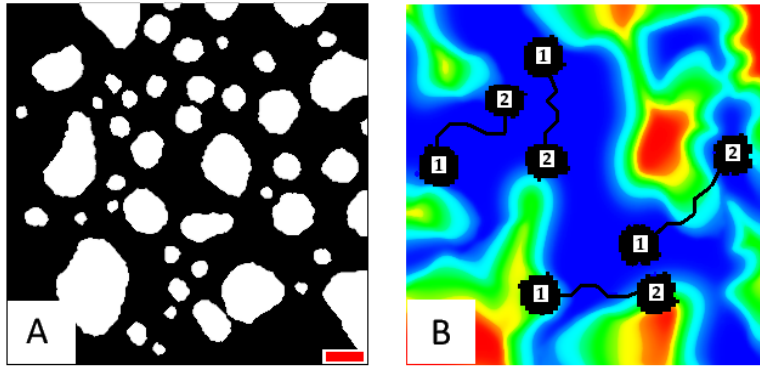


FIGURE 10. Inhibition of network organization by disrupting cell chemotactic response (i.e., imposing  $\mu_{ch}^i = 0$  for each  $i$  in Eq. (8)). In panel (A), we observe the formation of poorly differentiated vascular islands. As usually, the initial cell number is  $n = 150$  while all the other model parameters are the same of the basic simulation in Fig. 2. Red scale bar is  $100 \mu\text{m}$  long. Panel (B) reproduces the magnification of four representative single-TEC motion trajectories obtained from the time-lapse simulation. The initial (i.e., at 0 h) position of individuals is labeled with 1, while the final (i.e., at 12 h) with 2. Each segment tracks a displacement of 2 hours. In the background the concentration field of VEGF is pseudocolor-scaled so that the maximum level is red and minimum level is blue, as in Fig. 6. The motion of cells is uncorrelated from the directions of high VEGF concentration, as they do not experience the chemical force. Moreover, in the absence of the chemotactic stimulus, the individuals do not elongate, remaining in a stationary un-polarized morphology.

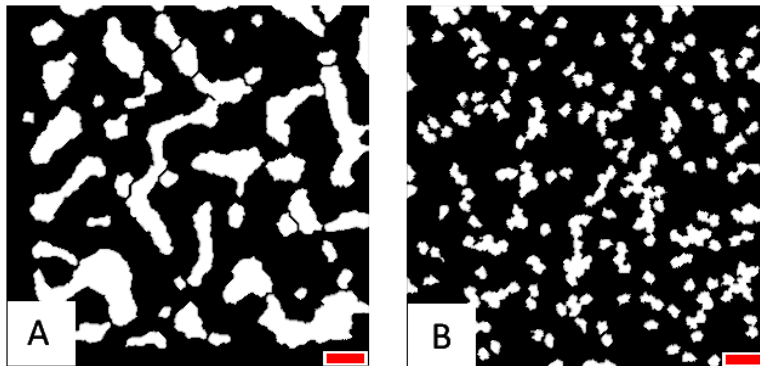


FIGURE 11. Inhibition of network organization by disrupting cell persistent movement (imposing  $\mu_{pers}^i = 0$  for each  $i$  in Eq. (10)), (A) panel, and cell-cell adhesive interactions (setting  $J_{C,C}^{ext} = 0$  for each cell-cell interface in Eq. (6)), (B) panel. In both case the initial cell number is  $n = 150$ , while all the other model parameters are the same of the basic simulation in Fig. 4. Red scale bar is  $100 \mu\text{m}$  long.

chemical stimulus, their membrane are in fact not able to protrude in a preferred direction, but isotropically fluctuate in the environs. The inhibition the cell persistent movement, with  $\mu_{pers}^i = 0$  for all  $i$  in Eq. (10), produces instead clumped, stunted and somewhat immature vascular sprouts. They are typically thick (3-4 cells wide) and characterized by large intervascular spaces, see Fig. 11A. Finally, the disruption of adhesive intercellular interactions (i.e.,  $J_{C,C}^{ext} = 0$  for each cell-cell interface in Eq. (6), the computational counterpart of anti-VE-cadherin antibodies) results in a dispersed cellular population, see Fig. 11B, as provided in [52] also for “normal” ECs.

**4. Discussion.** Vascular transition is a fundamental step in cancer development and consists of an intricate and multilevel network of driving mechanisms. In particular, a series of molecular events strongly regulates the behavior and interactions of tumor-derived endothelial cells, and, ultimately, their ability to organize in a vascular plexus. These events are largely mediated by angiogenic factors (such as VEGF isoforms [20]) and calcium plays an important role as a signal transducer [28, 58, 59, 61]. However, the process of malignant vascularization is still not fully clarified and a deep understanding of its multiscale events represents therefore a tremendous challenge in cancer treatment, giving rise to multiple experimental and computational models [3, 16].

In particular, different CPM works have provided a complete description of the minimal set of phenomenological processes required for the formation of a vascular network, see [51, 52, 53]. These approaches have been used as a useful starting point for the construction of a model which aimed at analyzing the component mechanisms of the patterning, not only at the cellular scale but also at the microscopic level. In order to achieve these insights, with respect to the above-cited models, we have made steps further both focusing on tumor-derived ECs and incorporating in the classical CPM approach a continuous model of their specific intracellular biochemical dynamics. For instance, the addition of the microscopic level has allowed us to derive the TEC biophysical properties and behavior from their evolving internal state, without the use of a set of *a priori* rules, which is common in literature. The resulting model has appeared to be quite successful in describing experimental results reproducing with a high level of confidence a TEC tubulogenic assay, with a number of parameters which are under control and biologically significant. The evolution of the cell culture has been evaluated until 12 h, which has allowed to provide a coherent comparison with the experimental counterparts. In particular, the final patterns reproduced in Figs. 4, 8, 10, and 11 have represented quasi-steady states of the system, as further iterations of the algorithm would have only resulted in negligible modifications of those morphologies. The system, in the absence of global minimum configurations in which stabilizing (they could not exist in our model because of the presence of the chemical and the persistence terms in the hamiltonian and, especially, of periodic boundary conditions in the domain), would have in fact fluctuated around the presented configurations, which were rather characterized by local energetic minima. The model has been able to characterize the geometrical properties of the tumor capillary plexus, suggesting its dependence on the cell density. An overcrowded population of malignant endothelial cells would in fact alter the development of a functional vasculature, while an initial cell number below a well-defined range is not permissive for the formation of a mature and structured network. Moreover, our simulations have predicted that an abnormal capillary-like

bed is also caused by the abrogation of cell chemotactic response, as well as of their persistence in motion and adhesive interactions. Such results could in principle give rise to potentially efficient biomedical strategies that aim at disrupting tumor vascularization [71]. In particular, along the text, we have underlined the model results which have been previously carried out for “normal” ECs, both experimentally and computationally. They have in fact represented an interesting parallelism between physiological and pathological vascularization and show how an accurate analysis of “normal” vessel formation is a fundamental starting point to interfere with its malignant counterpart.

However, our work contains a number of assumptions and limitations, that can be improved in several directions. Simplifications have been made at the molecular level to limit the number of biochemical interactions: we have used a minimal description of the VEGF-induced sub-cellular machinery underlying calcium events, which can be refined by providing both a finer degree of proangiogenic regulatory networks and more detailed structural and functional information on calcium channels and pumps. For instance, tumor-derived tubulogenesis has widely demonstrated to require the redundant action of multiple factors besides VEGF isoforms (i.e., acidic and basic fibroblast growth factors, epidermal growth factor, transforming growth factor- $\alpha$ , transforming growth factor- $\beta$  and several more, as reviewed in [25]). Moreover, the calcium-dependent pathway presented in this work is only one of the numerous cascades activated by VEGF itself [45]. Therefore, an analysis focused on these specific intracellular dynamics might be considered to have a little effect on the study of the overall malignant vascularization. However, most current drugs target the VEGF system, either by directly binding VEGF molecule to slow its diffusion down (see [45, 61, 75] and references therein) while calcium signals have been showed to be fundamental in malignant vascularization in a variety of tumors [59]. Indeed, given that no single *in silico* model could incorporate every aspects of every process involved in angiogenic progression, nor this level of complexity would be necessary for a mathematical approach to be useful or predictive, our choice to focus on VEGF-induced Ca-dependent protein networks has not represented a significant limitation, since it has followed the main lines of the research on cancer treatment. However, we strongly believe that a deep and differentiated understanding of the other multiple underpinning cellular and molecular events coordinated to control tumor-derived vessel formation would advance efforts aimed at the development of new therapies. At this regards, it is useful to underline that the proposed method to interface the basic CPM with the continuous model of microscopic dynamics does not apply only to this specific case but can be rather considered a general guide: it can be in fact easily adapted to other pathways of interest, given the equation (and the parameters) regulating the evolution of the chemicals and the functional laws describing their influence on the cells biophysical properties. A significative limitation of the approach is instead that, at the cellular level, several TEC basal properties have been derived only from a qualitative comparison with experimental cultures, even if they have been constrained in a range consistent with our own system, see Appendix for details: further selected experiments would therefore be useful for a better calibration of the model parameters. A further, natural development of the discrete CPM could be the incorporation of a description of the kinetics of the cytoskeletal remodeling. The present version of the model in fact does not focus on the dynamics of actin filaments, but rather considers the cell cytosol as a single elastic body undergoing local mechanical stresses, due

to thermodynamic forces and chemical stimuli, on its membrane. A more detailed multiscale model would use the stress distributions at the PM as a signaling input for the subsequent polymerization process of the actin cytoskeleton. Moreover, the introduction of the dynamics of the cell cytoskeleton would also result in a more accurate description of the movement of cell nucleus. In reality, the motility of the nucleus is characterized not only by the drag forces exerted by the surrounding cytosol, but also on one side by the interactions with the matrix substrate, mediated by the intermediate actin filaments and microtubules themselves, and on the other by autonomous thermodynamical fluctuations. Another fundamental improvement of our model is the explicit introduction of the interactions between cells and extracellular environment. First of all, we have not taken into account cell-matrix adhesion: however, even though it should obviously be included in a more detailed model, its exclusion has not strongly influenced the final outcomes of the approach. The contact interactions between vascular cells and homogenous and isotropic matrix substrates have been in fact demonstrated to play a major role in the stabilization of an *in vitro* vascular network, rather than in its early formation. In particular, the theoretical works presented in [2, 44], supported by the biological literature therein, have provided that the intercellular interactions and their chemotactic and persistent migration represent the minimal set of biological mechanisms sufficient to guarantee the emerging of the capillary structure. On the other hand, cell-ECM adhesion only sustains the preservation of its morphology under shear stresses and perturbations. Consistently, in [81], the traction/adhesion between the cell population and the gel layer starts acting when a sufficient density is locally obtained, i.e. when cells are no longer isolated but already connected. Indeed, cell-substrate adhesive strengths could dominate the early stages of vascular patterning only in extreme cases. As observed again by the authors of [81], a too strong cell-ECM adhesion inhibits the movement of cells, which remain isolated and dispersed in their initial position. An overly adhesive substrate causes in fact the formation of clusters of integrin-ligand bounds at cells surfaces, that do not detach, stopping further cell locomotion. On the contrary, a too weak cell-ECM adhesion results in the packing of cells in big islands, as they try to minimize the parts of their membrane in contact with the extracellular medium. Therefore, the exclusion of cell-matrix adhesion from our model is not too restrictive, since we focused on the initial formation of the network, and not on its following stabilization, and the implicit assumption that cell-matrix contacts are characterized by an intermediate strength. Following the same line of thoughts, the presented approach can be further developed with the inclusion of other interactions between the cell population and the substrate, that have been analyzed in other computational models. For instance, in [48], the movement of cells has been biased towards direction of principal strains of the underlying matrix, while in [62], the authors have added a cell sensitivity to matrix density gradients (i.e., the haptotactic mechanism) and long-range interactions in matrix stretching due to its fibrous nature. The mechanical and topological properties could also be characterized. For example, dense protein matrices, trapping a number of growth factor molecules, in fact slow morphogen diffusion and, causing steeper gradients, alter cell chemical responses, while anisotropic substrates drive cell migration and interfere with the network formation, especially in a three-dimensional patterning. More experiments, focused on the relevance of our findings, are then needed to shed light and validate our conclusions. Eventually, it would be also interesting the relevance of our results *in vivo*. However, in

this case, it would be very difficult to have a complete control of all the involved biological mechanisms, and there would be complications also due to the presence of other cells types [16, 19].

**5. Appendix - Parameter estimates.** Several parameters of our model have been taken from literature and are specifically referred to tumor-derived endothelial cells, others have been derived from experiments with different cell lines and experimental conditions. Finally, when a parameter value was not available, it has been estimated within reasonable biophysical constraints. A summary of parameters used has been done in Tables I and II while, in this Appendix, we will give details on how each estimate has been calculated.

The initial TEC dimensions are taken from literature, and represent the average measures of experimental cultures [28, 30]. Given the phenomenological nature of the CPM, a direct one-to-one correspondence between the CPM parameters describing the basal properties of TECs and the analogous experimental quantities is not straightforward (see also reviews [34, 54] for a comment). However, it is possible to realistically and accurately infer these values by deriving empirical relationships with *in vitro* measurements.  $T_0$  represents the high intrinsic of TECs and has been computed by comparing a simulated wound healing assay with its *in vitro* counterpart. The values in the parameter space that have lead to the optimal empirical fitting to experimental data in [28, 30] was  $T_0 = 4.5$ .  $T_N$  models instead the intrinsic motility of cell nucleus. In particular, low values of  $T_N$  translate into small nuclear membrane fluctuation, which is biologically reasonable (see Sec 3 for a detailed explanation). Indeed, as experimental data on nuclear membrane ruffles were not available, we have experimented a large range of values, before settling on a low value  $T_N = 0.25$ . Since we have not included in the model any nutrients, in order to keep fluctuations of cell volume within a few percent, after some trials we have used an high  $\kappa_0 = 20$ . Moreover, also the stochastic extensions and retractions of nuclear membrane have been widely demonstrated to be negligible: therefore the inverse compressibility of cell nuclei has been set to be an high  $\nu_N = 20$ .  $\nu_0$  represents the basal compressibility of the cell (i.e in the absence of any stimulation or mechanical force): observing that resting TECs maintained their initial configuration, with negligible changes of shape or cytoskeletal reorganization, we have chosen a moderate  $\nu_0 = 12$  [28, 30].  $J_{C,N}^{int}$  is the generalized contact tension between the nuclear subunit and the cytosolic region of each cell  $i$ . We have chosen an high  $J_{C,N}^{int} = -15$  to prevent TECs from disconnecting.  $J_0 = 5$  represents instead the low basal adhesive strength of TECs, which have been demonstrated to adhere only in confluence, see again [30].  $\mu_{ch,0}$  is the cell intrinsic chemotactic response: since biological measurements were not available, we have tried a wide range of low values and selected  $\mu_{ch,0} = 0.5$ , assuming that the chemical sensitivity of the cell is strongly increased by cytosolic calcium ions.  $\mu_{pers,0}$  represents instead the coefficient of cell directional persistence: we set  $\mu_{pers,0} = 1.2$ , which fits best experimental measure made on “normal” ECs in [53, 74].

VEGF secretion  $\phi_V = 0.78 \text{ h}^{-1}$ , diffusion  $D_V = 10 \text{ } \mu\text{m}^2\text{s}^{-1}$ , and decay  $\lambda_V = 1.8 \cdot 10^{-4} \text{ s}^{-1}$  have been quoted in [74].  $\beta_V$ , the maximal amount of VEGF molecules that can be locally bound by each TEC for unit of time has been estimated following [6, 47]. To avoid further complications, we have not taken into account time-dependent mechanisms, such as receptor recycling or clusterization. The diffusion and the inactivation rate of PKA, respectively  $D_P = 30 \text{ } \mu\text{m}^2\text{s}^{-1}$  and  $\lambda_P = 23 \text{ s}^{-1}$ ,

have been measured in [68], while the analogous values for AA,  $D_A = 10 \mu\text{m}^2\text{s}^{-1}$  and  $\lambda_A = 30 \text{s}^{-1}$  have been taken from [60], where they have been estimated fitting experimental measurements made by the same group on bovine aortic endothelial cells [56]. The intracellular NO diffusion has been taken to be  $D_N = 3300 \mu\text{m}^2\text{s}^{-1}$ , as calculated in [46], while the coefficient of NO degradation  $\lambda_N = 0.1 \text{s}^{-1}$  has been evaluated again in [60]. The Michaelis-Menten coefficients  $\alpha_A = 30 \mu\text{Ms}^{-1}$  and  $\beta_A = 1 \mu\text{M}$  of VEGF-mediated production of AA have been chosen for the best fit with experimental measures made in the same theoretical paper [60]. Since few data were available for the VEGF receptor-mediated activation of PKA and production of NO, and for the AA-induced PKA recruitment we have used  $\alpha_P = \alpha_N = \gamma_P = \alpha_A$  and  $\beta_P = \beta_N = \zeta_P = \beta_A$ . The production of NO regulated by AA, via PKA, has also been described by a classical Michaelis-Menten function:  $\gamma_N = 1.5 \mu\text{Ms}^{-1}$ , the maximal rate of NO release, has been estimated by fitting the time course of NO production experimentally measured using fluorescent probes and selective electrodes in [11, 30, 56], while  $\zeta_N = 0.5 \mu\text{M}$  has been taken from [66]. The intracellular resting cytosolic  $\text{Ca}^{2+}$  concentration has been assumed uniform for all cells, as  $C_0^i(\mathbf{x}) = C_0 = 0.05 \mu\text{M}$  for any sites  $\mathbf{x}$  of  $i$ , as well as the initial external calcium concentration of the ion,  $C_{ext,0}(\mathbf{x}) = C_{ext,0} = 2000 \mu\text{M}$ , following experimental [9] and theoretical [60] works. The calcium diffusion coefficient  $D_C = 220 \mu\text{m}^2\text{s}^{-1}$  has been well characterized in literature for several cell lines [27, 43, 60]. Several authors model the  $\text{Ca}^{2+}$  efflux as a sum of Hill functions [60, 82]. We have approximated this by a single Michaelis-Menten term, with coefficients  $k_C = 24.7 \mu\text{Ms}^{-1}$ , the maximal rate of extrusion, and  $C_{out} = 0.32 \mu\text{M}$ , the calcium concentration at which the rate of exchange is half maximal, chosen to fit those Hill-type curves over a physiological range of calcium concentration. The calcium entry through AA- and NO-sensitive channels has been described by saturable Michaelis-Menten relations, where  $F_{A,max} = 6 \text{s}^{-1}$  and  $F_{N,max} = 4.5 \text{s}^{-1}$  are the maximal influx rates, while  $q_A = 2 \mu\text{M}$  and  $q_N = 5 \mu\text{M}$  are the relative concentrations of second messengers responsible for the half maximal activation of the respective channels. All these parameters have been chosen to fit the calcium-permeable channel currents obtained by patch clamp experiments in [30, 56, 60]. The rates of buffering and debuffering of  $\text{Ca}^{2+}$  to intracellular proteins have been measured by several experimental works: in particular, we have used  $K_{on} = 100 \mu\text{M}^{-1}\text{s}^{-1}$  and  $K_{off} = 300 \text{s}^{-1}$  from [7]. The total concentration of calcium binding sites in the cytosol has instead been estimated to be  $b_T = 450 \mu\text{M}$ , accordingly to [27, 60].

**Acknowledgments.** MS was partially funded by the Italian Ministry of University and Research under a grant on “Math Models of the Interactions between Cells and Environment” and by Fondazione Credito di Risparmio di Torino (CRT) through a “Lagrange Project Fellowship”.

## REFERENCES

- [1] M. A. Albrecht, S. L. Colegrove and D. D. Friel, *Differential regulation of ER  $\text{Ca}^{2+}$  uptake and release rates accounts for multiple modes of  $\text{Ca}^{2+}$ -induced  $\text{Ca}^{2+}$  release*, J. Gen. Physiol., **119** (2002), 211–233.
- [2] D. Ambrosi, A. Gamba and G. Serini, *Cell directional persistence and chemotaxis in vascular morphogenesis*, Bull. Math. Biol., **66** (2004), 1851–1873.
- [3] D. Ambrosi, F. Bussolino and L. Preziosi, *A review of vasculogenesis models*, J. Theor. Med., **6** (2005), 1–19.



- [4] A. Balter, R. M. Merks, N. J. Poplawski, M. Swat and J. A. Glazier, *The Glazier-Graner-Hogeweg model: Extensions, future directions, and opportunities for further study*, in “Single-Cell-Based Models in Biology and Medicine, Mathematics and Biosciences in Interactions” (eds. A. R. A. Anderson, M. A. J. Chaplain and K. A. Rejniak), Birkhäuser, (2007), 157–167.
- [5] P. Baluk, S. Morikawa, A. Haskell, M. Mancuso and D. M. McDonald, *Abnormalities of basement membrane on blood vessels and endothelial sprouts in tumors*, *Am. J. Pathol.*, **163** (2003), 1801–1815.
- [6] A. L. Bauer, T. L. Jackson and Y. Jiang, *A cell-based model exhibiting branching and anastomosis during tumor-induced angiogenesis*, *Biophys. J.*, **92** (2007), 3105–3121.
- [7] P. Bayley, P. Ahlstrom, S. R. Martin and S. Forsen, *The kinetics of calcium binding to calmodulin: Quin 2 and ANS stopped-flow fluorescence studies*, *Biochem. Biophys. Res. Commun.*, **120** (1984), 185–191.
- [8] J. Bennett and A. Weeds, *Calcium and the cytoskeleton*, *Br. Med. Bull.*, **42** (1985), 385–390.
- [9] M. J. Berridge, M. D. Bootman and H. L. Roderick, *Calcium signalling: Dynamics, homeostasis and remodelling*, *Nat. Rev. Mol. Cell Biol.*, **4** (2003), 517–529.
- [10] M. J. Berridge, *Calcium signalling and cell proliferation*, *Bioessays*, **17** (1995), 491–500.
- [11] L. A. Blatter, Z. Taha, S. Mesaros, P. S. Shacklock, W. G. Wier and T. Malinski, *Simultaneous measurements of Ca<sup>2+</sup> and nitric oxide in bradykinin-stimulated vascular endothelial cells*, *Circ. Res.*, **76** (1995), 922–924.
- [12] M. D. Bootman, P. Lipp and M. J. Berridge, *The organisation and functions of local Ca<sup>2+</sup> signals*, *J. Cell. Sci.*, **114** (2001), 2213–2222.
- [13] B. Bussolati, M. C. Deregibus and G. Camussi, *Characterization of molecular and functional alterations of tumor endothelial cells to design anti-angiogenic strategies*, *Curr. Vasc. Pharmacol.*, **8** (2010), 220–232.
- [14] B. Bussolati, I. Deambrosio, S. Russo, M. C. Deregibus and G. Camussi, *Altered angiogenesis and survival in human tumor-derived endothelial cells*, *FASEB J.*, **17** (2003), 1159–1161.
- [15] B. Bussolati, C. Grange and G. Camussi, *Tumor exploits alternative strategies to achieve vascularization*, *FASEB J.*, **25** (2011), 2874–2882.
- [16] F. Bussolino, M. Arese, E. Audero, E. Giraudo, S. Marchio, S. Mitola, L. Primo and G. Serini, *Biological aspects in tumor angiogenesis*, in “Cancer Modeling and Simulation, Mathematical Biology and Medicine Sciences” (ed. L. Preziosi), Chapman & Hall/CRC, (2003), 1–16.
- [17] Y. Cao, H. Chen, L. Zhou, M. K. Chiang, B. Anand-Apte, J. A. Weatherbee, Y. Wang, F. Fang, J. G. Flanagan and M. L. Tsang, *Heterodimers of placenta growth factor/vascular endothelial growth factor. Endothelial activity, tumor cell expression, and high affinity binding to flk-1/kdr*, *J. Biol. Chem.*, **271** (1996), 3154–3162.
- [18] P. Carmeliet and R. K. Jain, *Angiogenesis in cancer and other diseases*, *Nature*, **407** (2000), 249–257.
- [19] P. Carmeliet, *Angiogenesis in life, disease and medicine*, *Nature*, **438** (2005), 932–936.
- [20] P. Carmeliet, *VEGF as a key mediator of angiogenesis in cancer*, *Oncology*, **69** (2005), 4–10.
- [21] P. D. Chilibeck, D. H. Paterson, D. A. Cunningham, A. W. Taylor and E. G. Noble, *Muscle capillarization O<sub>2</sub> diffusion distance, and VO<sub>2</sub> kinetics in old and young individuals*, *J. Appl. Physiol.*, **82** (1997), 63–69.
- [22] W. Coatesworth and S. Bolsover, *Calcium signal transmission in chick sensory neurones is diffusion based*, *Cell Calcium*, **43** (2008), 236–249.
- [23] K. De Bock, S. Cauwenberghs and P. Carmeliet, *Vessel abnormalization: Another hallmark of cancer? Molecular mechanisms and therapeutic implications*, *Curr. Opin. Genet. Dev.*, **21** (2011), 73–79.
- [24] C. J. Drake, A. LaRue, N. Ferrara and C. D. Little, *VEGF regulates cell behavior during vasculogenesis*, *Dev. Biol.*, **224** (2000), 178–188.
- [25] N. Ferrara, *VEGF and the quest for tumour angiogenesis factors*, *Nat. Rev. Cancer*, **2** (2002), 795–803.
- [26] N. Ferrara and R. S. Kerbel, *Angiogenesis as a therapeutic target*, *Nature*, **438** (2005), 967–974.
- [27] C. C. Fink, B. Slepchenko, Moraru, II, J. Watras, J. C. Schaff and L. M. Loew, *An image-based model of calcium waves in differentiated neuroblastoma cells*, *Biophys. J.*, **79** (2000), 163–183.
- [28] A. Fiorio Pla, C. Grange, S. Antoniotti, C. Tomatis, A. Merlino, B. Bussolati and L. Munaron, *Arachidonic acid-induced Ca<sup>2+</sup> entry is involved in early steps of tumor angiogenesis*, *Mol. Cancer Res.*, **6** (2008), 535–545.

- [29] A. Fiorio Pla and L. Munaron, *Calcium influx, arachidonic acid, and control of endothelial cell proliferation*, Cell Calcium, **30** (2001), 235–244.
- [30] A. Fiorio Pla, T. Genova, E. Pupo, C. Tomatis, A. Genazzani, R. Zaninetti and L. Munaron, *Multiple roles of protein kinase a in arachidonic acid-mediated  $ca^{2+}$  entry and tumor-derived human endothelial cell migration*, Mol. Cancer Res., **8** (2010), 1466–1476.
- [31] A. Fiorio Pla, H. L. Ong, K. T. Cheng, A. Brossa, B. Bussolati, T. Lockwich, B. Paria, L. Munaron and I. S. Ambudkar, *TRPV4 mediates tumor-derived endothelial cell migration via arachidonic acid-activated actin remodeling*, Oncogene, (2011), in press.
- [32] D. Fukumura, D. G. Duda, L. L. Munn and R. K. Jain, *Tumor microvasculature and microenvironment: Novel insights through intravital imaging in pre-clinical models*, Microcirculation, **17** (2010), 206–225.
- [33] A. Gamba, D. Ambrosi, A. Coniglio, A. de Candia, S. Di Talia, E. Giraud, G. Serini, L. Preziosi and F. Bussolino, *Percolation, morphogenesis, and burgers dynamics in blood vessels formation*, Phys. Rev. Letters, **90** (2003), 118101–118104.
- [34] J. A. Glazier, A. Balter and N. J. Poplawski, *Magnetization to morphogenesis: A brief history of the Glazier-Graner-Hogeweg model*, in “Single-Cell-Based Models in Biology and Medicine, Mathematics and Biosciences in Interactions” (eds. A. R. A. Anderson, M. A. J. Chaplain and K. A. Rejniak), Birkhäuser, (2007), 79–106.
- [35] J. A. Glazier and F. Graner, *Simulation of the differential adhesion driven rearrangement of biological cells*, Phys. Rev. E Stat. Phys. Plasmas Fluids Relat. Interdiscip. Topics, **47** (1993), 2128–2154.
- [36] Y. Goto, M. Miura and T. Iijima, *Extrusion mechanisms of intracellular  $Ca^{2+}$  in human aortic endothelial cells*, Eur. J. Pharmacol., **314** (1996), 185–192.
- [37] F. Graner and J. A. Glazier, *Simulation of biological cell sorting using a two-dimensional extended Potts model*, Phys. Rev. Lett., **69** (1992), 2013–2016.
- [38] C. Grange, B. Bussolati, S. Bruno, V. Fonsato, A. Sapino and G. Camussi, *Isolation and characterization of human breast tumor-derived endothelial cells*, Oncol. Rep., **15** (2006), 381–386.
- [39] A. C. Guyton and J. E. Hall, “Textbook of Medical Physiology,” 10<sup>th</sup> edition, W. B. Saunders, 2000.
- [40] L. V. Hryshko and K. D. Philipson, *Sodium-calcium exchange: recent advances*, Basic Res. Cardiol., **92** (1997), 45–51.
- [41] S. Huang, C. P. Brangwynne, K. K. Parker and D. E. Ingber, *Symmetry-breaking in mammalian cell cohort migration during tissue pattern formation: Role of random-walk persistence*, Cell Motil. Cytoskeleton., **61** (2005), 201–213.
- [42] H. Kimura and H. Esumi, *Reciprocal regulation between nitric oxide and vascular endothelial growth factor in angiogenesis*, Acta Biochim. Pol., **50** (2003), 49–59.
- [43] J. Klingauf and E. Neher, *Modeling buffered  $Ca^{2+}$  diffusion near the membrane: Implications for secretion in neuroendocrine cells*, Biophys. J., **72** (1997), 674–690.
- [44] R. Kowalczyk, *Preventing blow-up in a chemotaxis model*, Journal of Mathematical Analysis and Applications, **305** (2005), 566–588.
- [45] M. Kowanetz and N. Ferrara, *Vascular endothelial growth factor signaling pathways: Therapeutic perspective*, Clin. Cancer Res., **12** (2006), 5018–5022.
- [46] J. R. Lancaster, *A tutorial on the diffusibility and reactivity of free nitric oxide*, Nitric Oxide, **1** (1997), 18–30.
- [47] A. W. Mahoney, B. G. Smith, N. S. Flann and G. J. Podgorski, *Discovering novel cancer therapies: A computational modeling and search approach*, in “IEEE conference on Computational Intelligence in Bioinformatics and Bioengineering,” (2008), 233–240.
- [48] D. Manoussaki, S. R. Lubkin, R. B. Vernon and J. D. Murray, *A mechanical model for the formation of vascular networks in vitro*, Acta Biotheor., **44** (1996), 271–282.
- [49] A. F. M arée, V. A. Grieneisen and P. Hogeweg, *The Cellular Potts Model and biophysical properties of cells, tissues and morphogenesis*, in “Single-Cell-Based Models in Biology and Medicine, Mathematics and Biosciences in Interactions” (eds. A. R. A. Anderson, M. A. J. Chaplain and K. A. Rejniak), Birkhäuser, (2007), 107–136.
- [50] A. F. Marée, A. Jilkine, A. Dawes, V. A. Grieneisen and L. Edelstein-Keshet, *Polarization and movement of keratocytes: A multiscale modelling approach*, Bull. Math. Biol., **68** (2006), 1169–1211.
- [51] R. M. Merks and J. A. Glazier, *Dynamic mechanisms of blood vessel growth*, Nonlinearity, **19** (2006), C1–C10.

- [52] R. M. Merks, S. V. Brodsky, M. S. Goligorsky, S. A. Newman and J. A. Glazier, *Cell elongation is key to in silico replication of in vitro vasculogenesis and subsequent remodeling*, *Dev. Biol.*, **289** (2006), 44–54.
- [53] R. M. Merks, E. D. Perryn, A. Shirinifard and J. A. Glazier, *Contact-inhibited chemotaxis in de novo and sprouting blood vessel growth*, *PLoS Comput. Biol.*, **4** (2008), e1000163, 16 pp.
- [54] R. M. Merks and P. Koolwijk, *Modeling morphogenesis in silico and in vitro: Towards quantitative, predictive, cell-based modeling*, *Math. Model Nat. Phenom.*, **4** (2009), 149–171.
- [55] N. Metropolis, A. W. Rosenbluth, M. N. Rosenbluth, A. H. Teller and E. Teller, *Equation of state calculations by fast computing machines*, *J. Chem. Phys.*, **21** (1953), 1087–1092.
- [56] A. Mottola, S. Antoniotti, D. Lovisolò and L. Munaron, *Regulation of noncapacitative calcium entry by arachidonic acid and nitric oxide in endothelial cells*, *FASEB J.*, **19** (2005), 2075–2077.
- [57] L. Munaron, *Calcium signalling and control of cell proliferation by tyrosine kinase receptors (review)*, *Int. J. Mol. Med.*, **10** (2002), 671–676.
- [58] L. Munaron, *Intracellular calcium, endothelial cells and angiogenesis*, *Recent Patents Anticancer Drug Discov.*, **1** (2002), 105–119.
- [59] L. Munaron, C. Tomatis and A. Fiorio Pla, *The secret marriage between calcium and tumor angiogenesis*, *Technol. Cancer Res. Treat.*, **7** (2008), 335–339.
- [60] L. Munaron, *A tridimensional model of proangiogenic calcium signals in endothelial cells*, *The Open Biology Journal*, **2** (2009), 114–129.
- [61] L. Munaron and A. Fiorio Pla, *Endothelial calcium machinery and angiogenesis: Understanding physiology to interfere with pathology*, *Curr. Med. Chem.*, **16** (2009), 4691–4703.
- [62] P. Namy, J. Ohayon and P. Tracqui, *Critical conditions for pattern formation and in vitro tubulogenesis driven by cellular traction fields*, *J. Theor. Biol.*, **227** (2004), 103–120.
- [63] B. S. Parker, P. Argani, B. P. Cook, H. Liangfeng, S. D. Chartrand, M. Zhang, S. Saha, A. Bardelli, Y. Jiang, T. B. St Martin, M. Nacht, B. A. Teicher, K. W. Klinger, S. Sukumar and S. L. Madden, *Alterations in vascular gene expression in invasive breast carcinoma*, *Cancer Res.*, **64** (2004), 7857–7866.
- [64] A. M. Patton, J. Kassis, H. Doong and E. C. Kohn, *Calcium as a molecular target in angiogenesis*, *Curr. Pharm. Des.*, **9** (2003), 543–551.
- [65] E. D. Perryn, A. Czirik and C. D. Little, *Vascular sprout formation entails tissue deformations and VE-cadherin-dependent cell-autonomous motility*, *Dev. Biol.*, **313** (2008), 545–555.
- [66] J. S. Pollock, U. Forstermann, J. A. Mitchell, T. D. Warner, H. H. Schmidt, M. Nakane and F. Murad, *Purification and characterization of particulate endothelium-derived relaxing factor synthase from cultured and native bovine aortic endothelial cells*, *Proc. Natl. Acad. Sci. USA*, **88** (1991), 10480–10484.
- [67] N. J. Poplawski, A. Shirinifard, M. Swat and J. A. Glazier, *Simulation of single-species bacterial-biofilm growth using the Glazier-Graner-Hogeweg model and the CompuCell3D modeling environment*, *Math. Biosci. Eng.*, **5** (2008), 355–388.
- [68] J. J. Saucerman, J. Zhang, J. C. Martin, L. X. Peng, A. E. Stenbit, R. Y. Tsien and A. D. McCulloch, *Systems analysis of PKA-mediated phosphorylation gradients in live cardiac myocytes*, *Proc. Natl. Acad. Sci. USA*, **103** (2006), 12923–12928.
- [69] N. J. Savill and P. Hogeweg, *Modelling morphogenesis: From single cells to crawling slugs*, *J. Theor. Biol.*, **184** (1997), 118–124.
- [70] M. Scianna, *A multiscale hybrid model for pro-angiogenic calcium signals in a vascular endothelial cell*, *Bull. Math. Biol.*, (2011), in press.
- [71] M. Scianna, L. Munaron and L. Preziosi, *A multiscale hybrid approach for vasculogenesis and related potential blocking therapies*, *Prog. Biophys. Mol. Biol.*, **106** (2011), 450–462.
- [72] M. Scianna and L. Preziosi, *Multiscale developments of the Cellular Potts Model*, (2011), submitted for publication.
- [73] S. Seaman, J. Stevens, M. Y. Yang, D. Logsdon, C. Graff-Cherry and B. St Croix, *Genes that distinguish physiological and pathological angiogenesis*, *Cancer Cell*, **11** (2007), 539–554.
- [74] G. Serini, D. Ambrosi, E. Giraudo, A. Gamba, L. Preziosi and F. Bussolino, *Modeling the early stages of vascular network assembly*, *EMBO J.*, **22** (2003), 1771–1779.
- [75] F. Shojaei and N. Ferrara, *Antiangiogenic therapy for cancer: An update*, *Cancer J.*, **13** (2007), 345–348.
- [76] J. Sneyd, J. Keizer and M. J. Sanderson, *Mechanisms of calcium oscillations and waves: A quantitative analysis*, *FASEB J.*, **9** (1995), 1463–1472.

- [77] M. S. Steinberg, *Reconstruction of tissues by dissociated cells. Some morphogenetic tissue movements and the sorting out of embryonic cells may have a common explanation*, Science, **141** (1963), 401–408.
- [78] M. S. Steinberg, *Does differential adhesion govern self-assembly processes in histogenesis? Equilibrium configurations and the emergence of a hierarchy among populations of embryonic cells*, J. Exp. Zool., **171** (1970), 395–433.
- [79] O. Straume, H. B. Salvesen and L. A. Akslen, *Angiogenesis is prognostically important in vertical growth phase melanomas*, Int. J. Oncol., **5** (1999), 595–599.
- [80] C. Tomatis, A. Fiorio Pla and L. Munaron, *Cytosolic calcium microdomains by arachidonic acid and nitric oxide in endothelial cells*, Cell Calcium, **41** (2007), 261–269.
- [81] A. Tosin, D. Ambrosi and L. Preziosi, *Mechanics and chemotaxis in the morphogenesis of vascular networks*, Bull. Math. Biol., **68** (2006), 1819–1836.
- [82] P. A. Valant, P. N. Adjei and D. H. Haynes, *Rapid  $Ca^{2+}$  extrusion via the  $Na^{+}/Ca^{2+}$  exchanger of the human platelet*, J. Membr. Biol., **130** (1992), 63–82.
- [83] E. L. Watson, K. L. Jacobson, J. C. Singh and D. H. Di Julio, *Arachidonic acid regulates two  $Ca^{2+}$  entry pathways via nitric oxide*, Cell Signal, **13** (2004), 157–165.

Received January 2011; revised September 2011.

*E-mail address:* [marcosci1@alice.it](mailto:marcosci1@alice.it)

*E-mail address:* [luca.munaron@unito.it](mailto:luca.munaron@unito.it)